REDUCING RESIDUE IN NICKEL ELECTROPLATING OPERATIONS

A Thesis Submitted to the College of

Graduate Studies and Research

In Partial Fulfillment of the Requirements

For the Degree of M. Sc.

In the Department of Chemistry

University of Saskatchewan

Saskatoon

By

BURKE C. BARLOW

PERMISSION TO USE

In presenting this thesis in partial fulfillment of the requirements for a Postgraduate degree from the University of Saskatchewan, I agree that the Libraries of this University may make it freely available for inspection. I further agree that permission for copying of this thesis in any manner, in whole or in part, for scholarly purposes may be granted by the professor or professors who supervised my thesis work or, in their absence, by the Head of the Department or the Dean of the College in which my thesis work was done. It is understood that any copying or publication or use of this thesis or parts thereof for financial gain shall not be allowed without my written permission. It is also understood that due recognition shall be given to me and to the University of Saskatchewan in any scholarly use which may be made of any material in my thesis.

Requests for permission to copy or to make other uses of materials in this thesis/dissertation in whole or part should be addressed to:

Head of the Department of Chemistry

110 Science Place

University of Saskatchewan

Saskatoon, Saskatchewan S7N 5C9 Canada

OR

Dean

College of Graduate Studies and Research

University of Saskatchewan

107 Administration Place

Saskatoon, Saskatchewan S7N 5A2 Canada

ABSTRACT

Most commercial nickel electroplating cells use soluble nickel anodes that generate some amount of residue, typically nickel fines and impurities that detach from the bulk during normal operation. Build-up of residue over time leads to failure of the anode and necessitates shutdown and cleaning of the anode assembly before plating can resume. Of specific concern is the increase in plating residue from anode current densities less than 1 A dm^{-2} because as a consequence of cell design, the anode will often operate at a much lower current density than the cathode.

The electrodissolution of carbonyl nickel pellet, a commercial product for the electroplating market has been examined using electrochemical methods, coupled with *in situ* and *ex situ* microscopy to better understand the formation of anode residue. Applied potentials above the pitting potential resulted in current densities greater than 3 A dm^{-2} and pit interiors that were markedly different than those of galvanostatic pits at 0.4 A dm^{-2}. Current transients for potentiostatic pulses above the pitting potential were analyzed and the transition times for stages of pit growth were identified. A potential pulse sequence was then used to execute highly controlled cycles of pit nucleation, growth and repassivation that resulted in anode surface morphologies different than those treated galvanostatically. Potential pulse dissolution with a pulse time of 50 ms and 45% duty cycle gave a current density of 0.33 A dm^{-2} and resulted in more than a six-fold decrease in anode residue when compared to galvanostatic dissolution.

ACKNOWLEDGEMENTS

I would like to express my gratitude to my supervisor Dr. Ian Burgess, members of the Burgess group and my graduate committee members for their valuable discussions and guidance throughout my M. Sc. program. I would also like to thank my wife and parents for their continued support of my education.

I would like to acknowledge the financial support of the National Science and Engineering Research Council's Collaborative Research and Development Grant Program and industry partners Vale Canada Limited.

I would like to thank Grzegorz Szymanski from the Electrochemical Technology Center at the University of Guelph for performing the white light interference microscopy measurements.

TABLE OF CONTENTS

page

LIST OF TABLES

LIST OF FIGURES

LIST OF SYMBOLS AND ABBREVIATIONS

A	Surface area	q	Charge
a	Fitting constant	R	Gas constant
b	Fitting constant	RGB	Red, green, blue values
C_e	Electrode capacitance	R_s	Solution resistance close to electrode
C_i	Specific interfacial capacitance	r	Radius
c / $c_{j,b}$	Concentration / bulk concentration j	r_T	Transition radius
Δc_c	Cathode concentration drop during a pulse	SEI	Secondary electron imaging
Δc_p	Concentration change at planar boundary	SEM	Scanning electron microscope
CPT	Critical pitting temperature	STM	Scanning-tunneling microscopy
D	Diffusion coefficient	T	Absolute temperature
d_{crit}	Critical film thickness	T_p	Pulse time
E	Applied Potential	t	Time
$\mathbb{E}$	Electric field	t_p	Constant current density pit growth time
E_F	Flade potential	t_r	Pit repassivation time
E_p	Pitting potential	ΔU	Potential drop within a pit
F	Faraday's constant	V	Volume
FAA	Flame atomic absorption spectroscopy	V_M	Molar volume of metal
i	Current	WLIM	White light interference microscopy
i_p	Pit current density	XPS	X-ray photoelectron spectroscopy
J	Flux	Z_m / Z_j	Charge on the metal ion / species j
j	Electrode current density		
j_p	Pulsed current density		
K_h	Hydrolysis constant	α	Cathode efficiency fraction
k	Constant	γ	Surface tension
l	Anode to cathode distance	δ_N	Thickness of diffusion bilayer
M	Molar mass of Ni	δ_p	Thickness of pulsating diffusion layer
m	Mass of plated Ni	δ_s	Thickness of steady-state diffusion layer
$(p\text{-}p_o)$	Critical pressure to break film	ε	Dielectric constant of the passive film
PDM	Point-defect model	θ	Pulse cycle time
pH_b	pH of bulk electrolyte	κ	Solution conductivity
pH_p	pH of pit electrolyte	τ	Transient fitting time offset

CHAPTER 1

Introduction

1.1 Importance of Ni and Ni Plating

Nickel mining is the fifth most valuable mining industry in Canada with an annual production of 215 x 10^6 kg valued at $ 3.4 billion in 2013.[1] About 85% of all Ni production goes towards the fabrication of stainless steel and other Ni alloys that are ubiquitous throughout society.[2] Electrodeposited Ni coatings are commercially important with about 150 x 10^6 kg deposited annually in 2014, representing about 8-10% of all Ni use and 35-40% of all commercial electroplating worldwide.[2,3,4,5] Ni plating is found across all industries and for most applications there is no substitute.

Ni electrodeposits can generally be placed into three categories; decorative, functional or electroforming. Decorative applications consume roughly 80% of the Ni used for electrodeposition, while functional and electroforming applications consume the balance.[6] The majority of decorative Ni coatings are multi-layers deposited under a thin layer of Cr, a process known as chroming. Ni underlayers are deposited sequentially using slightly different electrolytes and conditions to impart a different level of corrosion resistance and brightness to each layer.[4.6] This process accounts for the majority of Ni electrodeposition in the auto industry and its application to substrates such as conductive plastic and aluminum has caused considerable growth in the area.[4,7] Functional Ni electroplating describes a wide variety of plating processes used to impart desired properties to the deposit when the appearance of the coating is not important. The scope of functional Ni coatings is immense due to the numerous desirable physical properties such as hardness, ductility, high melting point, high Curie temperature but most notably excellent corrosion resistance.[4,6] The third category of Ni electrodeposition is electroforming, which refers to the complete fabrication or reproduction of a part by electrodeposition. In this process Ni is deposited on a substrate, to which minimal bonding is desired and the deposit is later separated. Ni electroforming is an established route to very precise reproduction down to micron size scales and has been irreplaceable in the development of many 20th century technologies such as magnetic hard drive heads and compact

disk stampers.[4] The low tolerance of the fabricated parts is invaluable in the manufacture of high precision components for the aerospace and aircraft industry that must withstand demanding operating conditions. [4]

1.2 Technical Aspects of Ni Electroplating

1.2.1 Basics of Ni Electrodeposition

Ni electrodeposition, in the most basic terms, involves the submersion of two electrodes in a solution of Ni^{2+} salts and passing a current between them. Ni^{2+} is reduced and plated at the cathode, and oxidized and dissolved as Ni^{2+} at the anode. Under typical conditions there is a small amount of H_2 evolution and the efficiency at the cathode is less than 100%. Thus under normal operating conditions a gradual increase in Ni^{2+} concentration and pH is expected.[6] A simple diagram of a plating setup with anode and cathode reactions is shown in Figure 1-1. By application of Faradays law the mass of Ni deposited at the cathode, *m* can be approximated by the simple relation given in Equation 1.1, where *M* is the molar mass of Ni, *F* is Faradays constant of 96,500 C mole^{-1}, Z_M is the charge on the metal ion, *i* is the current in amperes and *t* is time in seconds. The proportionality constant, α is dictated by the cathode efficiency and should usually take values of 0.95 to 0.99.[6] The deposit thickness is then easily calculated using the density of Ni and the approximate surface area of the plated part.

$$m = \frac{\alpha M i t}{Z_M F} \qquad [1.1]$$

In order to approximate the mass of Ni and deposit thickness, the current or charge passed must be precisely measured. Most electroplating cells are run under direct current plating (also known as galvanostatic) conditions in which the current is kept constant by adjusting the cell potential. The deposit thickness is then easily estimated by simply monitoring the time. In this thesis direct current plating will be referred to as galvanostatic deposition/dissolution.

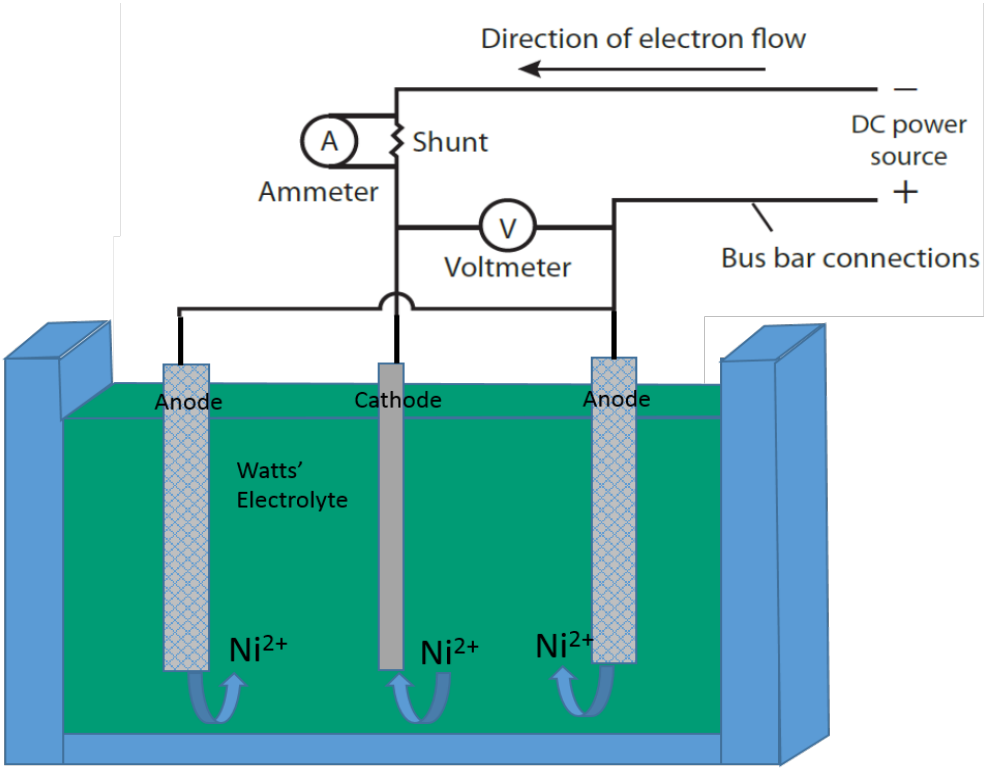

Anode:

$$Ni \longrightarrow Ni^{2+} + 2e^-$$

Cathode:

$$Ni^{2+} + 2e^- \longrightarrow Ni_{(s)} \quad > 95\%$$

$$2H^+ + 2e^- \longrightarrow H_{2(g)} \quad < 5\%$$

Figure 1-1: Diagram of typical Ni plating cell showing anode and cathode reactions.

1.2.2 Cell Design

The anode assembly generally consists of Ni anode material, a basket and a protective bag. Baskets are typically made from Ti mesh with reinforcing solid Ti strips at the top, bottom and edges and are suspended to contact the plating solution.[4,6] Their main function is to contain the Ni anode material and provide electrical contact between the Ni and the power supply. Encompassing the anode basket is a bag, made of a textile that is readily wetted by the electrolyte, allowing solution to flow while preventing any insoluble anode material from reaching the cathode.[4,6] Ti baskets are filled with Ni and topped up regularly to replace dissolved Ni and maintain a quasi-constant anode area. The basket itself will not corrode under normal operation as long as there is a sufficient supply of Ni loaded in the basket.[4,6] The rather

increased resistance of Ti compared to Ni means that Ti baskets must be mindfully designed such that resistance of the basket is minimized.[4,6]

The cathode assembly typically consists of racks or hooks for holding the substrates and are designed for minimum exposure of non-substrate surface to the plating electrolyte.[4] Because the exact deposit thickness at any point is proportional to the current at that point, the cathode surface is ideally equidistant from the anode at every point. Thus it is important to maintain a constant anode area and design the anode basket accordingly. In practice auxiliary anodes, insulating baffles and rotation of the cathode substrate are used to achieve a more evenly distributed current over the cathode surface.[4,6] It is important to note that generally the design of plating cells for optimum cathode deposit quality means the surface area of the anode basket will be many times that of the cathode.[4] In these cases, the current density at the anode will be a fraction of that desired at the cathode and anodes must operate satisfactorily at lower current density.

The remaining components of an electroplating cell are a power source (usually a direct current rectifier) and some form of agitation to ensure proper convection of solution throughout the tank. Agitation prevents density gradients in the tank and ensures the insulating $H_{2(g)}$ bubbles that form on the cathode are removed before they become large enough to affect the deposit.[4]

1.2.3 Ni Plating Electrolytes

The earliest historical report of Ni electroplating dates back to 1837 when Bird deposited Ni from a solution of Ni chlorides and sulfates.[8] The first widely used plating solution was developed by Bottger in 1843, and consisted of a mixture of Ni and ammonium sulfates.[9] This solution was widely used for the following 70 years until it was eventually replaced by Watts' electrolyte.

In 1916 Watts formulated a solution that combined $NiCl_2$ and $NiSO_4$ with H_3BO_3 at elevated temperatures to attain much higher current densities.[10] Although several other solutions are still used in lesser amounts, variations of Watts' formulation remain the most widely used electrolytes 100 years later, and the importance of his original formulation cannot be overstated. Typical composition and conditions of the electrolyte are given in Table 1. One other commercially important plating electrolyte utilizes $Ni(SO_3NH_2)_2$ as the primary source of Ni^{2+} and is generally used for a near-zero stress deposit for certain electroforming applications.[4,6]

Table 1: Watts' electrolyte composition and operating conditions.[4]

$NiSO_4\ 6H_2O$	240-300 g L^{-1} or 0.913-1.14M
$NiCl_2\ 6H_2O$	30 -90 g L^{-1} or 0.13-0.38M
H_3BO_3	30-45 g L^{-1} or 0.49-0.73M
Temperature	40-60^oC
pH	3.3-4.5

Nickel sulfate hexahydrate ($NiSO_4\ 6H_2O$) is present in Watts' electrolyte as the primary source if Ni^{2+} and is used due to its high solubility and low cost.[3] Nickel chloride hexahydrate ($NiCl_2\ 6H_2O$) provides a secondary source of Ni^{2+} however its main function is the specific action of Cl^- in pitting of the Ni anode surface. This is discussed in detail in Chapter 2 and will not be discussed further in this section. The presence of $NiCl_2\ 6H_2O$ also greatly increases the conductivity allowing a higher limiting current density at the cathode.[3,4,6] The much lower conductivity of $NiSO_4\ 6H_2O$ is attributed to the mass transfer of its solvated form. Higher concentrations of $NiCl_2\ 6H_2O$ permit a higher limiting current density but are often not ideal because deposit stress increases with increasing Cl^- concentration.[4,6] Therefore the concentration of Cl^- in Watts' electrolyte must be chosen with the desired deposit properties in mind.

Boric acid (H_3BO_3) is present in Watts' electrolyte as a buffer, however the buffering capability is not immediately evident because its lowest pKa is around 9.7.[11] As a general rule the buffering range of a solution species usually extends +/- 1 pH unit from its pKa. Since the ideal operating pH of Watts' electrolyte is less than 4.5, describing H_3BO_3 as a buffer is peculiar. It had been proposed that the buffering action is due to the formation of a solution complex between H_3BO_3 and Ni^{2+} in concentrated solution, however the existence of such a complex has since been debated.[12,13]

Tsuru et al used *in situ* near-surface pH monitoring and showed that surface pH did not increase at near limiting current density when the plating electrolyte contained 0.81 M H_3BO_3.[11] As the H_3BO_3 concentration was decreased, there was a pH increase at the cathode surface, which caused $Ni(OH)_2$ formation on the cathode. The increase in surface pH resulted from increased H_2 evolution that depleted H^+ near the cathode which was also evidenced by a large drop in current efficiency. In fact, for a plating electrolyte free of H_3BO_3, the cathode efficiency

dropped to 63%. Apparently the buffering action of H_3BO_3 arises from its ability to inhibit H_2 evolution at the cathode, which slows the removal of H^+ from the electrolyte.[11]

1.3 Nickel Anodes

Soluble Ni anodes serve two purposes, to provide the oxidation half of the total cell reaction and to replenish Ni^{2+} in the plating solution. The earliest and simplest anodes were electrolytic Ni strips of low purity that were suspended from hooks to contact the plating solution. There were several disadvantages with this type of anode including constantly changing size, uneven dissolution leading to fragmentation and waste. Perhaps the biggest drawback was that they were only available in certain lengths.[6] Around 1929, wrought depolarized Ni was the first anode material specifically developed to attain even dissolution.[6] It included a small amount of sulfur that increased the activity of the Ni and caused even dissolution, reducing fragmentation and waste. While macroscopic fragmentation was reduced, small metallic particles detached from the bulk and caused roughening of the cathode necessitating the use of anode bags.[14] Around 1938 wrought carbon anodes were developed and although they produced little metallic residue, small amounts of silicon and carbon in the material collected as insoluble films on the surface and required anode bags to keep it from contaminating the cathode.[15] While wrought anodes could be more easily fabricated to a variety of sizes they were still subject to constantly changing size because they were large single pieces. The use of large single piece anodes has been mostly replaced by small forms of high purity primary Ni.[6]

Modern Ni plating anodes are small forms of high purity (> 99%) Ni intended for use with Ti anode baskets. This practice overtook large single piece anodes because if properly maintained, the anode baskets have a near constant area for dissolution. Baskets can also be fabricated in many shapes and sizes to fit the needs of the cathode.[6] Many forms of primary Ni anode materials are available including pellets or chips obtained by chemical vapour deposition, and discs, and cubic pieces made via electrorefining.[6] Two basic compositions are commercially available, low-sulfur or sulfur-activated. Sulfur-activated Ni contains a small amount of sulfur that promotes even dissolution at low potentials. For certain electroforming applications sulfur-activated Ni is used without Cl^-, however in Watts' electrolyte, Cl^- induced pitting is the mechanism of dissolution and low-sulfur (unactivated) Ni anode material is used. Commercially

available low-sulfur Ni P-pellets, made by chemical vapour deposition of $Ni(CO)_{4(g)}$ are investigated in this work.

1.4 Ni Refining by Chemical Vapour Deposition

First reported by Mond in 1895, the reaction of $Ni_{(s)}$ with $CO_{(g)}$ and subsequent decomposition to produce high purity Ni has been widely used since its commercialization several years later.[16] Due to the extreme toxicity of $Ni(CO)_{4(g)}$ and $CO_{(g)}$ (permissible exposure limits of 1 ppb and 10 ppb respectively) the process must be operated in a closed system reactor with strict safety requirements. As a result of these toxicities, other gases have been investigated as possible replacements. However, $Ni(CO)_{4(g)}$ remains the most widely used due to its mild decomposition temperature and the high purity of the deposit that can be obtained.[17] The commercial process is comprised of the following reactions.[18]

$$NiO_{(s)} + H_{2(g)} \longrightarrow Ni_{(s)} + H_2O_{(g)} \quad 350\text{-}450\ ^oC \quad (1.1)$$

$$Ni_{(s)} + 4\ CO_{(g)} \longrightarrow Ni(CO)_{4(g)} \quad 50\text{-}60\ ^oC \quad (1.2)$$

$$Ni(CO)_{4(g)} \longrightarrow Ni_{(s)} + 4\ CO_{(g)} \quad \sim 200\ ^oC \quad (1.3)$$

Impure NiO is treated at elevated temperatures with $H_{2(g)}$ to produce elemental Ni plus other base metals. $CO_{(g)}$ is then passed over the Ni in the form of a fine powder at a temperature of 50-60 ^oC producing $Ni(CO)_{4(g)}$. The gaseous product is distilled to separate any $Fe(CO)_{5(g)}$ that may also form in the carbonylation vessel. $Ni(CO)_{4(g)}$ then enters a decomposition chamber with other feed gases where it decomposes on a Ni substrate that has been preheated to a decomposition temperature in the range of 230-280 ^oC.[18] Ideally the decomposition reaction should take place around 200 ^oC,[19] however to prevent Ni from depositing on the reactor itself, its temperature must be considerably lower and the substrate must be heated above 200 ^oC. $CO_{(g)}$ is liberated at the Ni surface and is collected and recycled through the process. Ni substrates, in the form of small seed particles, are introduced to the decomposition reactor and pass through many times, growing layer-by-layer until they reach sufficient size that they are expelled from the cycle.[18]

The process is considered environmentally benign because $CO_{(g)}$ is recycled through the process indefinitely, and it has relatively low energy requirements when compared to electrorefining.[18]

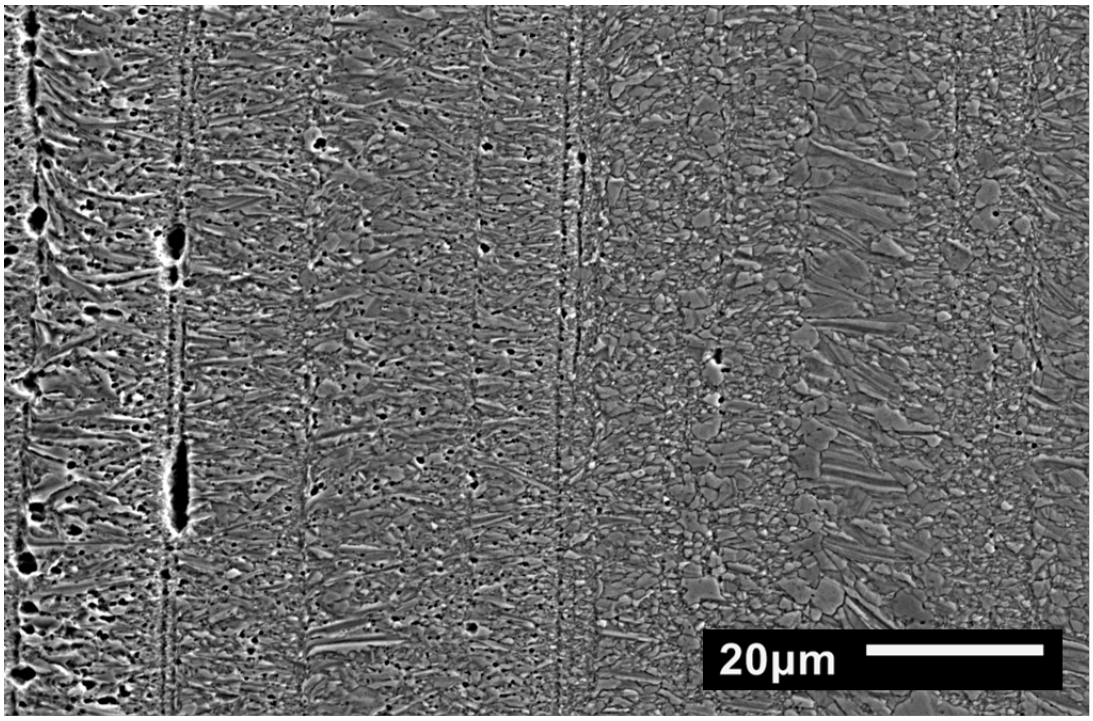

Figure 1-2: Etched Ni p-pellet cross section near the outer pellet edge showing distinct growth layers and long needle-like grains. The growth direction is right to left.

The texture and morphology of the deposit can vary widely within the decomposition temperature-gas concentration process window.[19,20] At a low concentration of feed gas and/or low temperature, the reaction is slowed such that it is not mass transport limited and a fine grain structure is produced.[20] On the other hand if the temperature is increased then the surface reaction becomes mass transport limited resulting in large columnar grains with a preferred growth direction.[20] Figure 1-2 shows a cross sectional scanning electron microscope (SEM) image of the grain structure of an etched carbonyl p-pellet, where the layer-by-layer growth is clearly visible. The growth direction is from right to left and the far left of the image corresponds to growth layers that are within 100 µm from the outer surface of the sphere. In general, long needle-like grains can be observed near the pellet surface and are indicative of the structure as deposited. However, they are not observed nearer to the center of the pellet maybe due to their

coalescence from repeated heating cycles. It has been shown that notable changes in the grain structure of carbonyl Ni probably do not happen at temperatures below 300 ^{o}C.[21]

1.5 Anode Residue

Anode residue, as it will be defined for this thesis, refers to any portion of a Ni anode that detaches from the bulk and sediments on any part the anode assembly. Residue may be captured by the anode bag or alternatively settle on any metallic surface of the anode assembly. Residue that redeposits on the Ni or Ti basket does not electrodissolve under normal cell operation even though electrical contact is made.[22,23] While anode residue represents a very low mass percentage of the anode material, it is problematic due to its accumulation on the anode assembly eventually causing failure.[22,23] A significant increase in residue necessitates more frequent maintenance where plating must be halted and the anode assembly must be cleaned before plating can resume. While research into carbonyl decomposition conditions has recently been shown to effect the dissolution behavior and residue levels,[19,24] precise control of electrochemical variables may offer an alternative route to mitigation of residue. Some preliminary research into the dissolution behavior that produces higher amounts of residue had already been completed at the beginning of this thesis research and the results will be presented next.

Controlled galvanostatic dissolution of single carbonyl pellets had been investigated previously using an electrode current density of 0.4 A dm^{-2}, which corresponds to the low anode current density that would occur in a typical plating setup. Anode current densities in this range are linked to a significant increase of anode residue. Figure 1-3 shows the evolution of a polished p-pellet cross-section after 30 minutes and 16 hours of dissolution in panels a) and b) respectively.[25] The appearance of the surfaces is similar despite panel b) corresponding to 32-fold more dissolution. A cross section of this sample is shown in Figure 1-3 c) and illustrates the depth to which the pitting has progressed. The deepest pit has grown to a depth more than ten times the size of the pit opening and its growth is highly irregular. Although this pitting is perpendicular to the electrode surface, it corresponds to dissolution along a specific ring of the electrode structure due to the cross sectional nature of the electrode. For a spherical shape this corresponds to pitting lateral to the surface.

a)

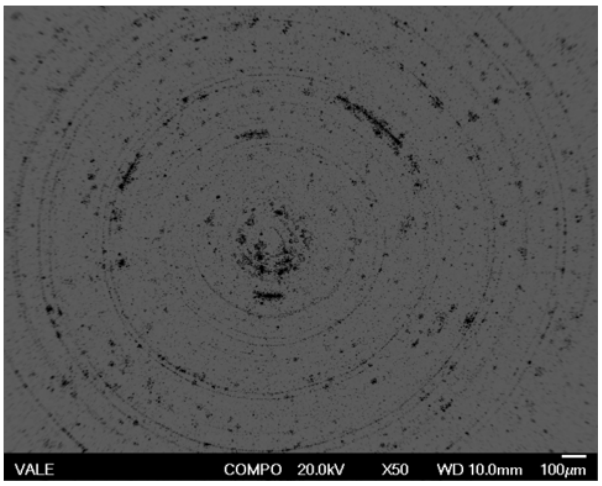

b)

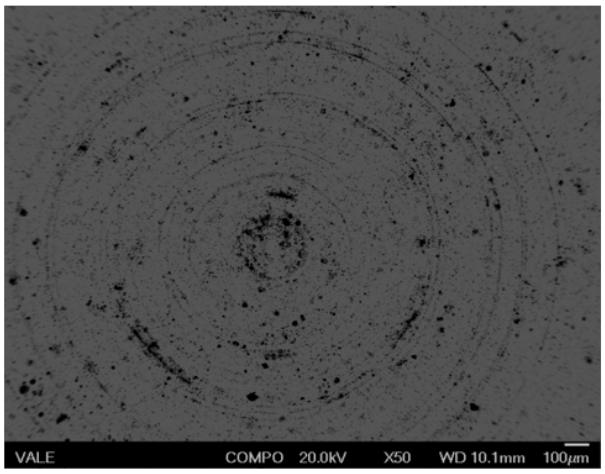

c)

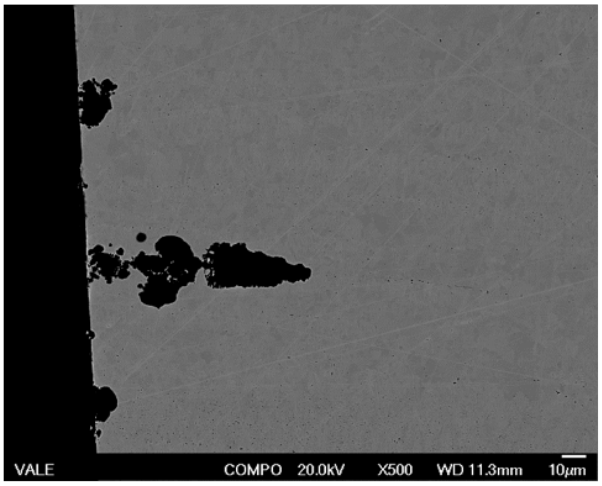

Figure 1-3: Ni p-pellet cross section after dissolution at 0.4 A dm^{-2}. Panel a) and b) show 30 minutes and 16 hours of dissolution respectively. Panel c) shows a cut through the center of b) showing growth perpendicular to the cross sectional surface along a specific growth layer.

Whole pellets were also subjected to dissolution at the same current density to examine the pitting behavior for a spherical geometry. The results of three trials are shown in Figure 1-4 that show p-pellet cross sections corresponding to 16 hours, 60% mass and more than 90% mass dissolution in panels a) through c) respectively.[25] Figure 1-4 d) shows the outer surface of a pellet after more than 90% mass dissolution. After 16 hours, the amount of Ni dissolution represents only a small percentage of the original anode mass. Some pits appear hemispherical with metallic covers while others have begun to propagate along a specific ring of the pellet structure. After 60% mass loss, the dissolution has progressed leaving behind a series of voids separated by thin walls enclosed in a thick walled outer shell. After more than 90% mass dissolution this mechanism has left behind only a skeleton of the original sphere. As can be seen in Figure 1-4 d) a large portion of the outer shell of the sphere remains pristine, while most of the inner pellet has dissolved. This skeleton of Ni is likely to fracture under the weight of Ni loading in the Ti basket and it is suspected that some portion of the skeleton should end in residue.[25] Due to the small particle size and soot-like appearance of carbonyl anode residue, it is also hypothesized that small fines readily detach from the bulk metal throughout the dissolution and make up a significant portion of the residue.

1.6 Research Objectives

This thesis research has essentially two main objectives, to examine the electrodissolution of Ni p-pellets over a range of potentials and their corresponding current densities in an effort to elucidate causes of anode residue, and to investigate whether precise control of electrochemical variables can reduce anode residue. Since it has already been established that anode residue decreases as current density is increased in galvanostatic experiments, control of electrochemical variables should be done in such a way that a low average anode current density (< 1 A dm^{-2}) can be realized.

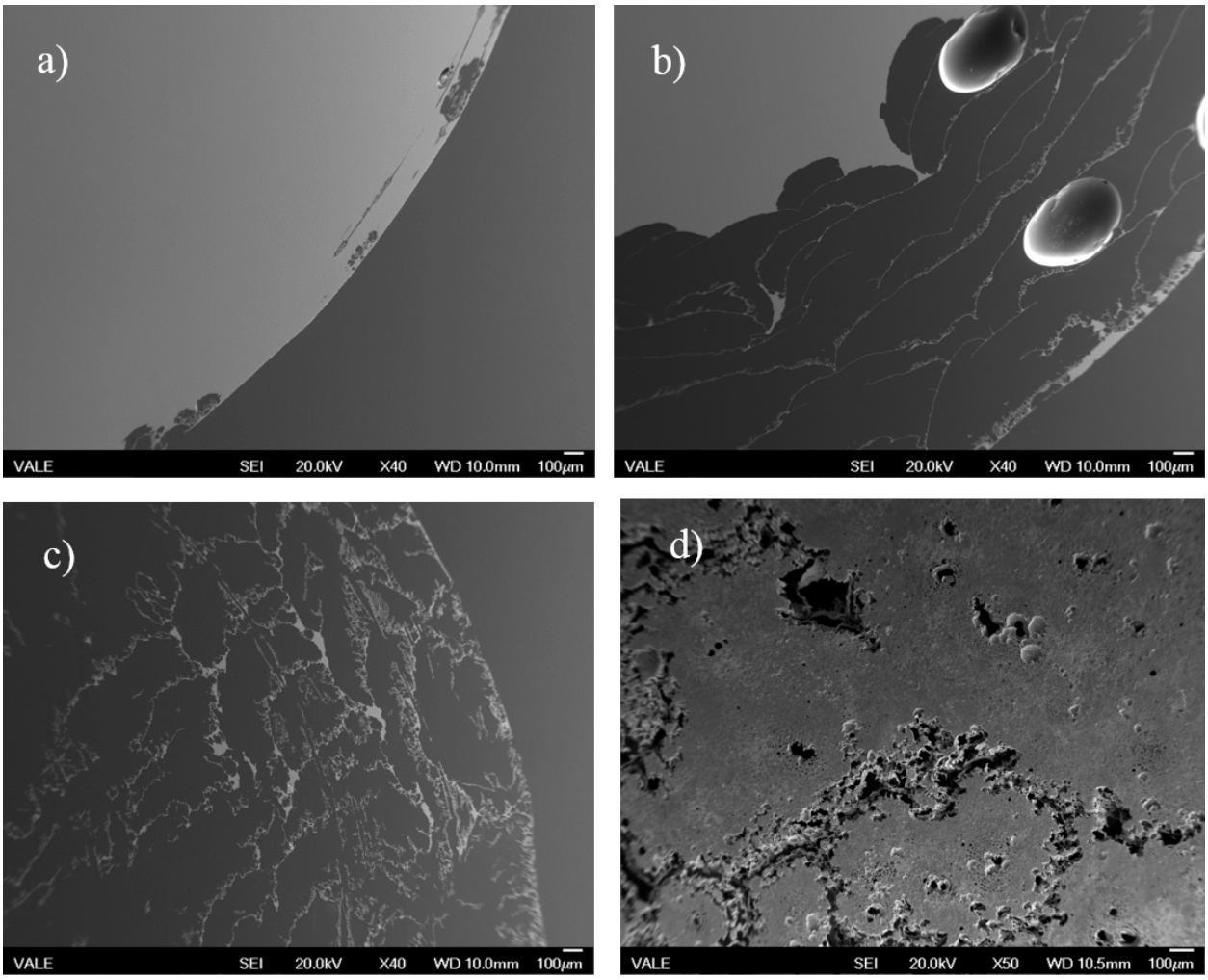

Figure 1-4: SEM images of whole Ni p-pellet dissolution at 0.4 A dm^{-2}. Panels a) through c) show cross sections of the pellet taken after dissolution corresponding to 16 hours, 60% mass, and > 90% mass dissolution respectively. Panel d) shows the intact outer surface of a spherical pellet after > 90% mass dissolution.

1.7 References

[1] Facts and Figures of the Canadian Mining Industry. https://mining.ca/sites/default/files/documents/Facts_and_Figures_2014.pdf (accessed May 2016)

[2] Nickel Metal – The Facts. https://nickelinstitute.org/NickelUseInSociety/AboutNickel/NickelMetaltheFacts.aspx (accessed May 2016)

[3] Whittington, C.; Rose, I. *Nickel Plating Handbook*; Nickel Development Institute: Brussels, 2014.

[4] Parkinson, R. *Nickel Plating and Electroforming- Essential industries for today and the future*; Nickel Development Institute: Brussels, NiDI Technical Series No. 10 088.

[5] Lampke, T.; Steger, H.; Zacher, M.; Steinhauser, S.; Wielage, B.; *Materialwissenschaft und Werkstofftechnik,* **2008**, *39*, 52.

[6] DiBari, G.A.; Electrodeposition of Nickel. In *Modern Electroplating, 5th Ed;* Schlesinger, M.; Paunovic, M. Eds; John Wiley & Sons: Hoboken, NJ, 2010; pp 79.

[7] Snyder, D.L.; *Metal Finishing,* **1997,** *95*, 29.

[8] Bird, G.; *Philos. Trans.*, **1837**, *127*, 37.

[9] Bottger, R. *Erdmann's J. Praktische Chemie,* **1843**, *30*, 267.

[10] Watts, O.P. *Trans. Am. Electrochem. Soc.,***1916**, *29*, 395.

[11] Tsuru, Y.; Nomura, M.; Foulkes, F.R. *J. Appl. Electrochem.,* **2002**, *32*, 629.

[12] Saubestre, E.B. *Plating,* **1958**, *45*, 927.

[13] Tilak, B.V.; Gendron, A.S.; Mosoiu, M.A. *J. Appl. Electrochem.* **1977** 7, 495.

[14] Wesley, W.A. *Trans. Inst. Met Finish,* **1956**, *33*, 452.

[15] Wenderott, B. *Metalloberflache* **1963**, *17*, 169.

[16] Mond, L. *J. Soc. Chem. Industries* **1895**, *14*, 945.

[17] Brissonneau, L.; Vahlas, C. *Ann. Chem. Sci. Mat*, **2000,** *25,* 81-90.

[18] Vale-University Consortium on Nickel Vapometallurgy, Sheridan Park, Mississauga 2012.

[19] Morrison, A.S.; Moula, G.; Barlow, B.C.; Burgess, I.J.; Shobeir, B.; Huang, H.; Lipkowski, J. *submitted to Electrochimica Acta,* **2015.**

[20] Pierson H.O. *Handbook of Chemical Vapour Deposition*; Noyes: New York, 1999.

[21] Chichi Chen M.Sc. Thesis. University of Toronto 2011.

[22] DiBari, G.A. In *Proc. 4th Int. Congress on Surf. Tech.;* AMK Berlin: Berlin, 1987.

[23] Whittington, C.M.; Yeung, K.L.K.; Lo, W.Y. *Transaction of the Institute of Metal Finishing*, **2011**, *89*, 122.

[24] Moula, M.G.; Szymanski, G.; Shobeir, B.; Huang, H.; Burgess, I.J.; Chen, A,; Lipkowski, J. *Electrochimica Acta,* **2015**, *162*, 108.

[25] Huang, H. Controlled Dissolution of Carbonyl P-Pellets. June 24, 2013.

CHAPTER 2

Theory and Literature Review

2.1 Introduction

Pitting corrosion refers to a process occurring at a metal surface covered by a passive film, where an area begins to corrode but remains surrounded by passive surface. Pitting corrosion requires exposure to a sufficient concentration of aggressive species and generally the aggressive species is chloride. The pitting potential E_p, represents the minimum potential for a given system that will lead to the propagation of stable, continually propagating pits. At a minimum, any pitting corrosion theory must be reconciled with the experimentally determined dependence of this potential on the concentration of aggressive species [Cl^-], according to Equation 2.1 where *a* and *b* are constants that depend on the exact nature of the system.[1]

$$E_p = a - b\log[Cl^-] \qquad [2.1]$$

Below E_p, only metastable pits are possible and by definition they will repassivate, generally within a few seconds. Once a pit is stably propagating, it may continue to grow for extended periods of time and it is in this stage that it is highly destructive. The ubiquity of Cl^- and the destructive nature of pitting corrosion of steels that are used throughout society have lead to extensive research on the subject. Most research is carried out with the goal of mitigating the damage of pitting corrosion, whereas in the case of this thesis, because Ni dissolution only occurs at high rates through a pitting mechanism, the aim will be to control pitting using electrochemical variables.

This chapter will establish pitting corrosion theory and background as it applies to Ni plating where corrosion pits supply nearly all of the anodic current. Literature references will be for Ni in a Cl^- containing electrolyte whenever possible, however the large number of publications regarding Fe based alloys, mainly stainless steels, means that some of the literature references will pertain to these materials. While the exact chemistry is obviously different, much of the background and theory should be satisfactorily extended to the pitting corrosion of Ni because many of the general mechanisms of passive-layer breakdown and pit growth have been extended to many corrosion systems throughout the literature.

The first step in the formation of a corrosion pit is local failure of the passive layer protecting the metal surface. Despite a considerable number of theories and models for passivity breakdown, it remains probably the least understood aspect of pitting corrosion.[2] To date no complete theory has been proposed that can account for all measurable phenomena. A single theory must account for the existence of E_p and the effect of aggressive and inhibiting ions on E_p, the localized nature of pitting, the existence of a temperature dependent induction period, film thickness and potential as well as the existence of metastable pits below E_p.[2] Since pitting is preceded by passivity breakdown, it is logical to first examine the passive film itself.

2.2 Passivity of Nickel

2.2.1 Passive Layer Formation

The excellent corrosion resistance of Ni is due to a $NiO/Ni(OH)_2$ bilayer passive film that forms on the Ni surface. X-ray photoelectron spectroscopy (XPS) experiments have followed passive film formation by analysis of the O 1s spectra at 25 ^{o}C after exposure to molecular oxygen.[3] Adsorbed O_2, atomic O and O^{2-} were identified, consistent with the mechanism proposed by Mott and Cabrera where O_2 adsorbs on the Ni surface and decomposes to atomic O.[4] After decomposition the interaction between Ni and O is covalent in nature, resulting in a dipole that facilitates a place exchange between the two atoms forming the first layer of oxide. Subsequent layers are formed by electron tunneling from the bulk metal to a second layer of adsorbed oxygen, generating an electric field that drives cation diffusion. At ambient temperatures, the kinetics are logarithmic and growth slows rapidly as the passive film thickens and the electric field decreases. Comparison of reaction rates between Ni(100) and polycrystalline samples revealed that polycrystalline metal is more reactive owing to higher cation diffusivity along grain boundaries in the substrate metal.[3]

Passive film formation by H_2O on polycrystalline Ni has been studied similarly and takes place by the same mechanism at a much reduced rate, owing to the slower place exchange between Ni and hydroxide ions.[5] The resulting film is thinner than those formed from O_2 because the growth is thought to terminate once all metallic Ni sites have reacted. Although OH bonds were detected in the film, $Ni(OH)_2$ and NiOOH were not present. Apparently the $Ni(OH)_2$ overlayer found on air oxidized Ni requires the presence of both O_2 and H_2O.

According to the electrochemical equilibrium diagram for Ni in weakly acidic media at anodic potentials, the thermodynamic tendency is for dissolution of metal into divalent Ni ions.[6] From a thermodynamic perspective, the passive layer is not stable below pH 8 and passivity is a kinetic phenomenon.[1] For Ni in acidic solution, the passive film is in a constant state of dissolution and reformation, with the reformation reaction dominating kinetically. A schematic for the proposed electrochemical formation of the passive layer in acidic solution is given by the following reaction sequences.[7]

$$Ni_{(s)} + H_2O \rightleftharpoons Ni(H_2O)_{(ad)} \rightleftharpoons Ni(OH)_{ad} + H^+_{(aq)} + e^- \qquad (2.1)$$

$$Ni(OH)_{(ad)} \rightleftharpoons Ni(OH)^+_{(ad)} + e^- \qquad (2.2)$$

$$Ni(OH)^+_{(ad)} + H_2O \longrightarrow Ni(OH)_{2(ad)} + H^+_{(aq)} \qquad (2.3a)$$

$$Ni(OH)_{2(ad)} \rightleftharpoons NiO_{(ad)} + H_2O$$

$$Ni(OH)^+_{(ad)} \rightleftharpoons Ni(OH)^+_{(aq)} \qquad (2.3b)$$

$$Ni(OH)^+_{(aq)} + H^+_{(aq)} \rightleftharpoons Ni^{2+}_{(aq)} + H_2O$$

In the first step, water adsorbs on the surface and dissociates as Ni undergoes a one-electron oxidation. The adsorbed Ni(OH) then undergoes another one electron oxidation to form the adsorbed cation. At this stage the adsorbed cation can react with an additional water, giving $Ni(OH)_2$ and then subsequently discharge a water molecule forming NiO (reaction 2.3a). Alternatively, the cation may desorb from the surface and react with a solution proton forming Ni^{2+} and water. In chloride-free electrolyte, the dominating reaction sequence for step 2.3 depends on potential and the transition can be observed in the current response as potential is made increasingly anodic. A typical current response for this situation is illustrated in Figure 2-1 for a Ni electrode, free of surface oxide (ie reduced *in situ* in deaerated solution). Active dissolution occurs at the least anodic potential where reaction path 2.3b is favoured over 2.3a and the current peak observed corresponds to Ni^{2+} dissolution. At a characteristic potential an inflection point is observed signaling the beginning of passive layer formation. This potential is most often called the Flade potential and is noted in Figure 2-1 as E_F. At this point reaction path

2.3a dominates and a NiO layer forms on the electrode surface. Although the passive layer is not in equilibrium the dissolution rate is reduced compared to the active region and the current is small. The passive film will remain over a large potential window until it is further oxidized at sufficiently positive potential and dissolves due to the formation of soluble Ni species that are produced at very positive potentials.[1] This causes the current to increase in a region called the transpassive region. In the presence of aggressive species such as Cl^-, large currents from the formation of stably propagating pits will occur before the onset of the transpassive region as indicated by the E_p region in Figure 2.1.

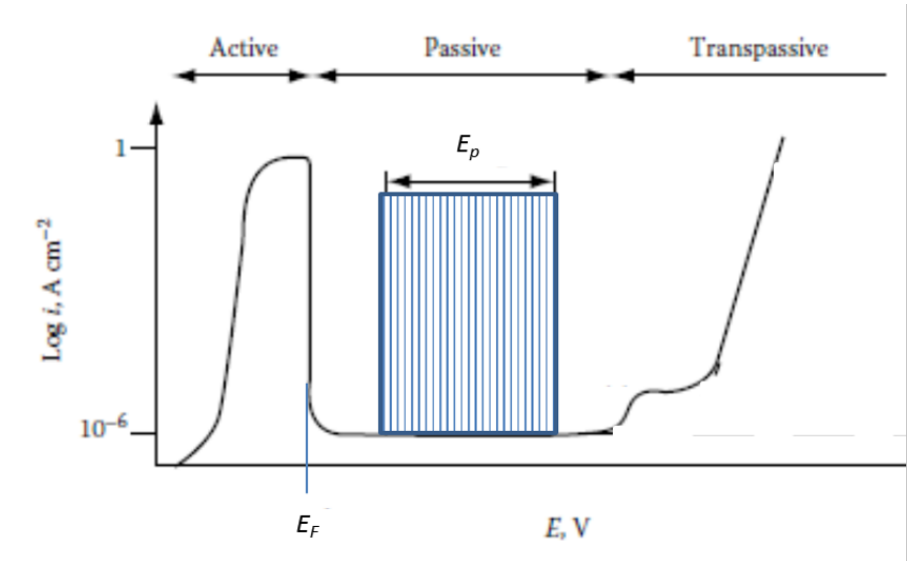

Figure 2-1: Typical current response for Ni in Cl- free acidic electrolyte showing active, passive and transpassive regions. In the presence of Cl-, the region labeled E_p indicates that pitting will start at potentials cathodic of the transpassive region.

2.2.2 Passive Layer Structure

The passive film on Ni has a bilayer structure consisting of an inner layer of NiO and an outer layer of $Ni(OH)_2$.[1,8,9] The total thickness of the layer has been reported between 0.9 nm and 1.2 nm for acid solution and up to 2.5 nm for alkaline solution, however similar values in acid and alkaline solution have also been reported.[8-10] In some cases the thickness has been reported to increase with increasing potential,[9,10] while others have found the thickness to be

independent of potential.[11]It is generally agreed that the NiO layer provides the corrosion resistance while the $Ni(OH)_2$ outer layer acts as an exchange layer with the electrolyte.[1]

Zuili et al separately imaged both layers of the structure formed electrochemically on Ni(111) in acid solution using *in situ* scanning tunneling microscopy (STM).[8] A model of their structure is shown in Figure 2-2. The inner NiO layers were crystalline with a stepped terrace structure corresponding to alternating planes of Ni^{2+} and O^{2-} with a separation of 0.12 nm and terraces ranging from 2-6 nm wide. A tilt angle of 3 +/- 1 ^{o} with respect to the substrate was approximated from the terrace width and confirmed by grazing angle x-ray diffraction. Atomic resolution showed hexagonal symmetry with a lattice constant of 0.3 +/- 0.03 nm, consistent with (111)-oriented NiO. This orientation is in agreement with previous *in situ* measurements,[11] however larger tilt angles of 6-15^{o} have also been reported.[13] The terrace size, lattice constant and tilt angle remained constant as the thickness of the layer increased with increasing passivation potential. When examined *ex situ*, the electrochemically formed NiO layer showed similar tilt and lattice structure. An air formed oxide layer was also examined *in situ* and was consistent with those formed electrochemically.[8]

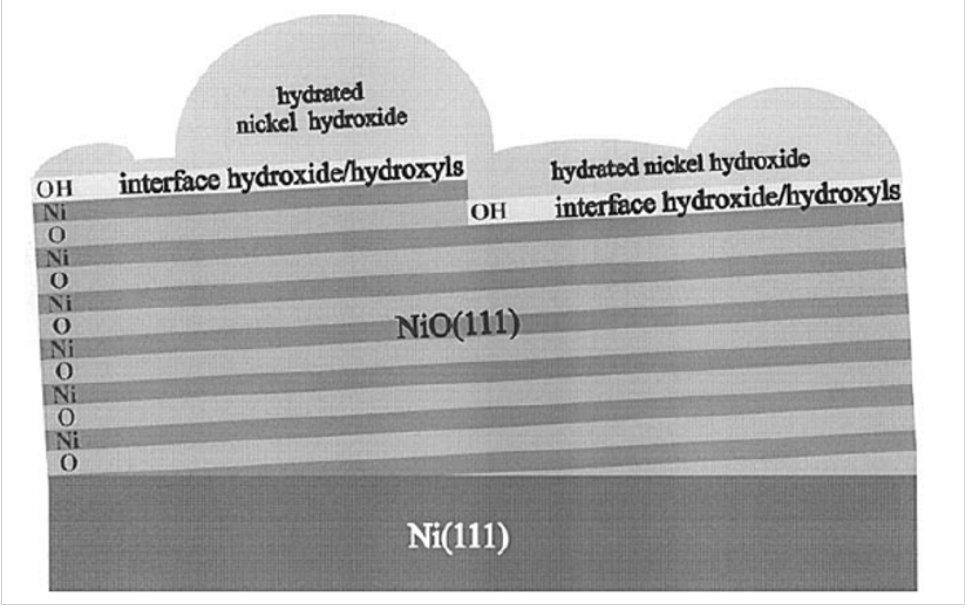

Figure 2-2: Diagram of the bilayer passive film formed on Ni(111) in acid solution. Reprinted with permission from reference 8. Copyright 2000, The Electrochemical Society

The extent of $Ni(OH)_2$ overlayer coverage has been reported for a number of different conditions, and ranges anywhere from a fraction of a monolayer,[9,14] up to full monolayer coverage.[11,15] *In situ* STM of the $Ni(OH)_2$ layer in acid solution revealed it was amorphous, with granular features ranging from 2-8 nm in size.[8] There was a marked increase in the grain size and roughness of the $Ni(OH)_2$ surface after aging the electrode at passive potentials, however increasing the potential had no measurable effect on the thickness of the $Ni(OH)_2$ layer. The amorphous nature of the layer was determined from the absence of an atomic lattice at high magnifications. Previous *ex situ* measurements had found the hydroxide layer to be crystalline and it is believed that incorporation of water causes disruption of the crystalline order.

2.2.3 Location of Cl^- in the Passive Layer

Marcus and Herbelin examined the location and entry of Cl^- in the passive layer on polycrystalline and single crystal Ni using spectroscopic and radioisotope methods.[11] A Ni electrode was reduced *in situ* and scanned anodically through the active and passive regions of polarization up to the pitting potential. In the active region, a three-dimensional NiCl(OH) layer formed on the electrode preceding passive film formation. At the active-passive transition region a sharp decrease in the surface concentration of Cl^- was observed concurrent with passive film formation, however a small amount of Cl^- was found irreversibly trapped at the Ni/NiO interface after formation of the film. Chloride was also found in the outer layer but in a chemically different state than in the active region. Incorporation of Cl^- in the outer layer of the film was the result of a limited exchange between Cl^- and OH^-. In this case it was calculated to be around 10% of the total surface OH^- sites at a bulk Cl^- concentration of $5x10^{-3}$ M. No entry of Cl^- into the NiO layer was observed until the potential approached the pitting potential. This result was verified by prepassivating an electrode in Cl^- free electrolyte followed by exposure to Cl^-. Furthermore, the concentration of Cl^- in the outer layer of the passive film was identical to that of the passive layer formed in the presence of Cl^-. At the pitting potential, an increase in concentration was measured within the passive film corresponding to an average concentration of $1x10^{-3}$ mol cm^{-3}. This concentration, by nature of the measurement is the average over the entire electrode surface and local extremes are generally accepted.

Several other examinations of Cl^- entry into the passive layers on metals and alloys have concluded that it does enter the passive film at potentials below E_p. The contradictory results can

be explained in terms of sample preparation and sensitivity of the method.[1] In the most careful works, Cl^- was found incorporated only in the outer hydroxyl layer of the film.

2.3 Passivity Breakdown

Three main mechanisms of passivity breakdown will be presented here. There remains no consensus as to which mechanisms dominate for various metals, alloys and aggressive species. However, it is generally agreed that some combination of these three can satisfactorily explain most experimental results.

2.3.1 Adsorptive Thinning

This mechanism makes the conjecture that the action of thinning species is to enhance the transfer rate of metal cations from the oxide to the electrolyte through a chemical reaction that produces an adsorbed surface complex. Since this transfer step is the rate-determining step of passive film dissolution, it leads to increased rates of dissolution. For localized removal of the passive layer, the rate of dissolution must become faster than reformation at a specific site. As the passive layer is thinned, the field strength across it increases, which increases migration through the film and can further accelerate passivity breakdown.[16,17]

Direct experimental evidence for the increased dissolution of the passive film has been obtained by comparing passive current densities for a Fe electrode exposed to SO_4^{2-} and ClO_4^-. The passive current density was one order of magnitude higher for SO_4^{2-} and attributed to the increased dissolution of the surface complex $FeSO_4^+$.[18] In this case the reformation reaction directly compensated the increased dissolution and the passive layer was not removed.[18]

Ni electrodes exposed to F^- undergo considerable thinning of the oxide over time, and in the presence of organic acids such as formic acid the NiO layer can be thinned or completely removed.[1,18,19] For Ni in F^- containing electrolytes, the attack is measureable however it is not localized. Strehblow and Marcus provide an explanation for this and suggest that localized passivity breakdown should not be attributed to adsorptive thinning because species that lead to a large increase in passive current density will adsorb evenly over the entire surface.[1]

Seo et al proposed that each site of Cl^- agglomeration on the passive film had a critical potential above which dissolution could occur.[20] Increased Cl^- adsorption at higher bulk Cl^-

concentration should lead to a lower pitting potentials. While this model offered an explanation for the dependence of E_p on the Cl^- concentration, it predicted that a thinner film should pit more rapidly than a thicker film, which was contradicted by later results. These results also showed that for a thinner film more charge must pass prior to the onset of pitting.[21,22] A general illustration of the adsorptive thinning model is shown in Figure 2-3 with metal, oxide and electrolyte indicated as Me, Ox and El respectively.

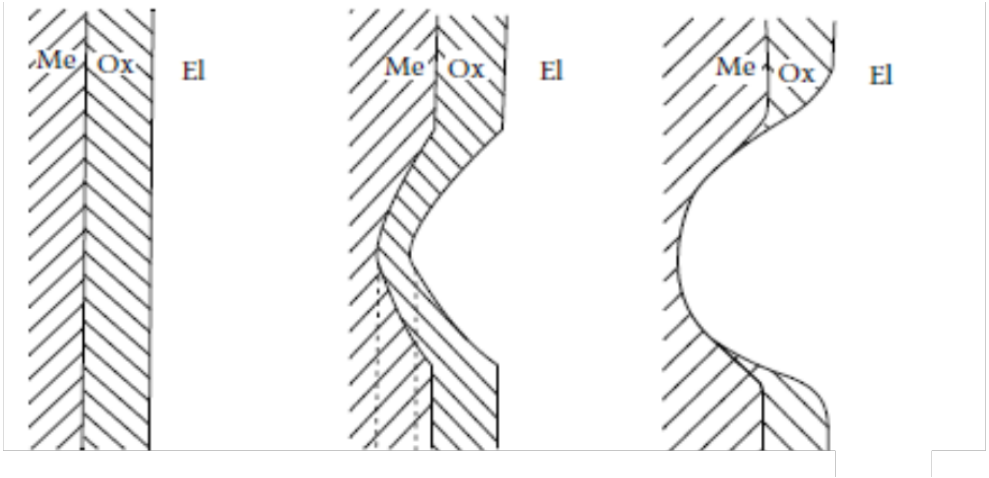

Figure 2-3: Diagram of adsorptive thinning mechanism showing passive layer dissolution that is faster than reformation resulting in eventual loss of the passive film. Metal, oxide and electrolyte are labeled Me, Ox and El respectively. Reprinted from reference 2 with permission from Elsevier.

2.3.2 Penetration Mechanism

First described by Hoar, the original mechanism considered that Cl^- penetrated the passive layer due to the large electric field across it.[23] A large number of localized defects in the film corresponded to regions of high ionic diffusivity and explained local breakdown of the film. Later Evans suggested that E_p for a penetration mechanism is the minimum field strength required for Cl^- penetration, and the induction time represents the time needed for penetration through the oxide film.[24]

In light of studies showing that Cl^- probably does not enter the NiO layer of the passive film at potentials below E_p, the point defect model (PDM) was developed around the idea that cation vacancies actually penetrate the film. PDM considers the specific role of Cl^- is to increase

cation vacancy generation at the film-electrolyte interface. First proposed by Chao et al, the mechanism is depicted in Figure 2-4 and can be summarized as follows.[25] Chloride incorporates into anion vacancies leading to increased cation vacancy generation at the film/electrolyte interface. Cation vacancies migrate toward the metal surface, driven by the large electric field. If their annihilation rate is insufficient, they will condense and form a void where the oxide layer detaches from the metal substrate. As the void grows, the oxide thins, eventually causing rupture of the unsupported film and a pit nucleus. The local nature of passivity breakdown is addressed by considering that clusters of defect sites with high vacancy flux are localized on the surface. Since the vacancy flux is dependent on the applied potential and the annihilation rate is rather independent of potential, an increase of potential will cause voiding at more sites and the density of pit nuclei on the surface should increase. Cation vacancy generation in NiO has been found to be first order with respect to Cl^- in agreement with experimental evidence that shows metastable pit nucleation rate is also first order with respect to Cl^-.[26] PDM can satisfactorily address certain phenomena that cannot be explained with an absorptive thinning model, such as the supra-bandgap photo-inhibition of pitting and explanation of halide size effects, and inhibiting effect of NO_3^-.[1] More recently Lu et al have examined previously published metastable pitting data for a variety of metal substrates and found PDM was able to predict the nucleation of metastable pits based on Cl^- concentration, pH and applied potential. On the basis of their model for metastable pit nucleation, they predicted that nearly all of the pits should nucleate shortly after the appearance of the first pit. They also concluded that for some systems where the concentration of Cl^- and/or the potential is high, the nucleation of the pits on the metal surface could be regarded as instantaneous nucleation because the first pit should appear at very short times.[27] The utility of PDM across many corrosion systems continues to strengthen the case for this model. However, there are some criticisms, specifically its inability to explain certain experimental results.[1] For example when a cathodic potential step is applied to a passivated Fe electrode, it causes an increase in corrosion current in less than a millisecond. In this case, the decreased electric field across the passive layer should reduce flux and nucleation should slow.[1] A third type of mechanism for passivity breakdown is needed to explain this result.

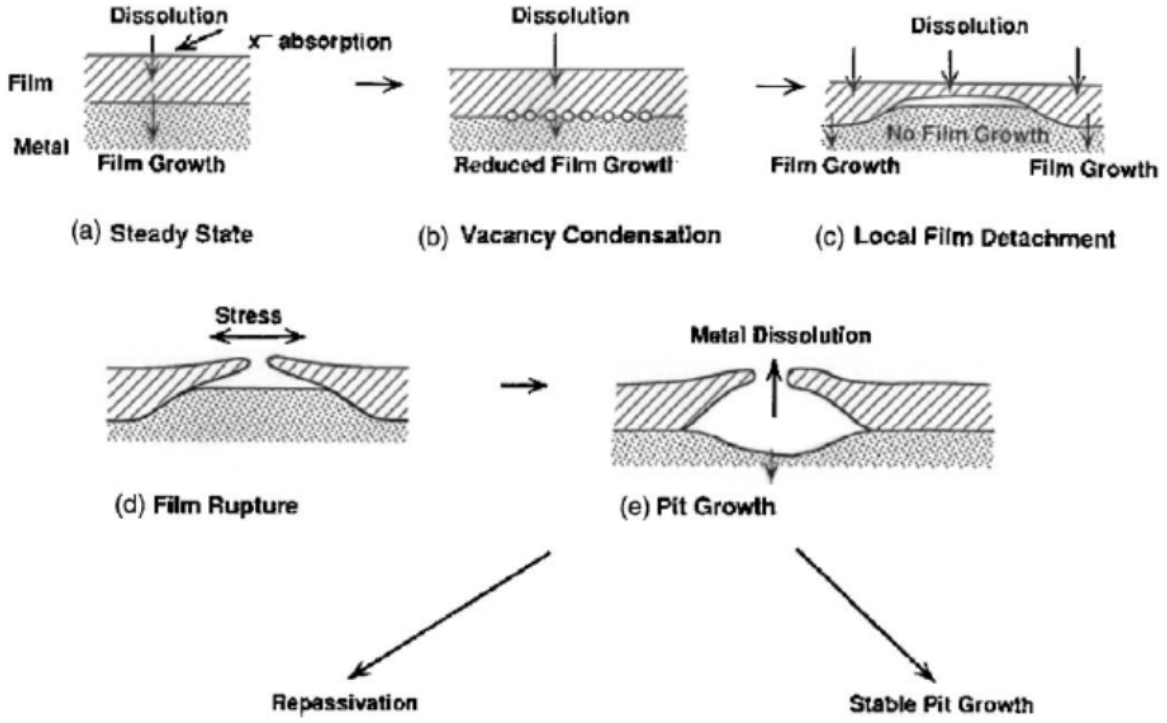

Figure 2-4: Diagram of the stages of passive layer breakdown by point-defect model. Reprinted with permission from reference 26. Copyright 2005, The Electrochemical Society

2.3.3 Film Breaking Mechanism

The film breaking mechanism considers that stresses in the film will cause its rupture at weak sites, momentarily exposing the metal to electrolyte as shown in Figure 2-5. In some views the passive layer is in a continuous state of breakdown and repair below E_p in the absence of Cl^-. Conversely, stresses may be created due to changes in potential (electrostriction), the adsorption of aggressive ions or salt precipitation at the metal-film interface. In general terms, film-breaking theories do not specifically require Cl^- to play a role in film breakdown events but only in the development of corrosion pits. Once exposure of the bare metal to Cl^- containing electrolyte occurs, Cl^- inhibits the reformation of the passive film.

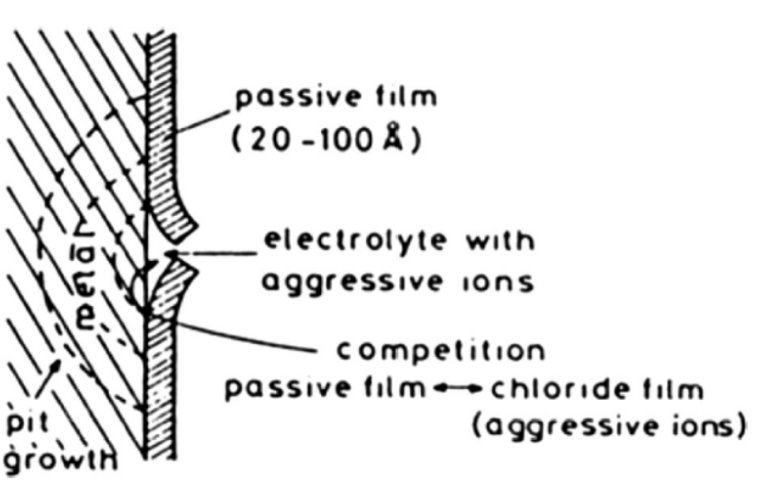

Figure 2-5: Depiction of film breaking mechanism leading to pitting. Reprinted from reference 2 with permission from Elsevier.

Under conditions of non-stationary potential, electrostrictive stress can cause rupture of the film at weak points. Direct experimental evidence for electrostrictive film breaking was obtained for passive films on Fe.[28] In this case a large cathodic potential step generated a momentary flux of Fe^{2+} from a Fe electrode that was subsequently detected in the form of a reduction current at a Pt-ring electrode surrounding the disk. Under these experimental conditions, Fe^{2+} can only originate from the exposure of bare Fe to electrolyte.[28] An explanation of this result using PDM is not possible because a cathodic step should lead to decreased cation vacancy flux. For Ni electrodes, measurable corrosion currents were observed less than 1 ms after the potential was stepped anodic of the pitting potential and were found to be inconsistent with PDM due to the extremely short induction time.[19]

Several authors have proposed that a stressed film is constantly rupturing and repairing at fixed potentials below the pitting potential.[29-33] In this case the pitting potential is the potential at which there is sufficient energy for the metal surface to become activated. Once the activated metal surface is exposed to Cl^-, it prevents repassivation by blocking the adsorption of passive film forming species.

The origin of the passive current has been attributed to the summation of many picoamp current pulses that arise from passive film breaking and repair processes occurring over the metal surface even when pitting is not observed.[31,32] Riley et al measured current pulses occurring at a much higher frequency than pitting nucleation and attributed them to individual film breaking

events that did not form pits.[33] In light of more recent work on electrochemical noise in corrosion systems, the origin of these fluctuations has been questioned by Lu et al, noting that a number of possible phenomena can give rise to such a measurement and causal determination is difficult.[27]

Another related mechanism requires that Cl^- ions play a distinctive role in film breaking by stressing the film. Hoar initially proposed that the adsorption of Cl^- onto the outer surface of the passive layer changed the surface tension of the film and caused film breakdown.[34] A thermodynamic treatment was subsequently published that calculated the surface pressure acting on the film according to Equation 2.2.[35] The critical pressure required to break the film, $(p-p_o)$ depends on the electric field, $\mathbb{E}$, surface tension, γ, and film thickness, d_{crit}. They supposed that the adsorption of Cl^- lowered γ, and increased the probability of film breaking at constant potential and film thickness. Similarly at a constant surface tension (ie constant Cl^- concentration), a thinner film required less field strength to cause its rupture. If local extremes of Cl^- adsorption are considered, large critical pressure differences are expected across the film and localized breakdown should be expected.

$$p - p_o = \frac{\varepsilon(\varepsilon-1)\mathbb{E}^2}{8\pi} - \frac{\gamma}{d_{crit}} \qquad [2.2]$$

The formation of metal halide salt films beneath the passive layer has been proposed as another route to passive film breaking on stainless steel.[36] Since the molar volume of the metal halide salt is much larger than that of the substrate metal or oxide, expansion would cause passive film rupture. Dissolution of the salt without formation of a pit was thought to be the origin of the picoamp fluctuations that make up the passive current for cases when pitting was not present.[2] For Ni, this mechanism leads to an apparent contradiction with the work of Marcus and Herbelin because it requires that Cl^- penetrate the NiO layer at potentials below E_p.[11]

2.4 Pitting

2.4.1 Relating Pit Current, Pit Radius and Time

Prior to a discussion on the growth of corrosion pits, relationships between the current, pit radius and time for two limiting cases of hemispherical growth need to be presented. In the first case, the growth of the pit is controlled by the flux *through* the pit opening. In the second

case, it is controlled by the flux from the pit interior. The following section deals with a pit under diffusion control. However, as will be discussed later the same dependencies are expected for pit growth that is ohmically-controlled.

In order to establish the time dependence for the two limiting cases, one first needs an expression relating the current to the growth of the pit radius in time. The charge passed during metal dissolution is directly proportional to the volume of metal dissolved, as per Equation 2.3 where q is the charge, V is the volume of metal dissolved, Z_m is the charge on the metal ion, F is Faradays constant and V_m is the molar volume of the metal.

$$q = \frac{Z_m F}{V_m} V \qquad [2.3]$$

Differentiating Equation 2.3 with respect to time gives Equation 2.4 describing the pit current, i.

$$\frac{dq}{dt} = i = \frac{Z_m F}{V_m} \frac{dV}{dt} \qquad [2.4]$$

Substituting the expression for the volume of a hemisphere into Equation 2.4 gives Equation 2.5, relating the current to the rate of change of the pit radius.

$$i = \frac{2\pi Z_m F}{3V_m} \frac{dr^3}{dt} \qquad [2.5]$$

The flux of species away from the electrode, J is related to the current by Equation 2.6, where A is the surface area generating the flux.

$$i = JZ_m FA \qquad [2.6]$$

The two possible cases described above are now considered. In case 1, the flux from the pit is constant while for case 2, the flux is limited by the pit interior and varies according to Fick's first law for radial diffusion.

Case 1

Since the flux is constant across the pit mouth, the current should vary with the two-dimensional surface area of the pit opening. The surface area of the pit opening is substituted for A in Equation 2.6 to obtain Equation 2.7.

$$i = JZ_m F\pi r^2 \qquad [2.7]$$

Since Equations 2.5 and 2.7 describe the current, equating them leads to Equation 2.8, which is integrated to give Equation 2.9 that describes the radius with time.

$$\frac{2}{3V_m}\frac{dr^3}{r^2} = Jdt \qquad [2.8]$$

$$r = \frac{JV_m t}{2} \qquad [2.9]$$

Finally, substituting Equation 2.9 into Equation 2.7 gives Equation 2.10, which describes the pit current in time.

$$i = kt^2 \qquad \text{where} \quad k = \frac{\pi Z_m F J^3 V_m^2}{4} \qquad [2.10]$$

The pit current for case 1 is expected to increase with t^2 while it is clear from Equation 2.9 that *dr/dt* is constant. It should also be noted that if Equation 2.7 is divided by the pit surface area, the pit current *density* is constant.

Case 2

In this case the flux from the pit varies according to Equation 2.11, which is Fick's first law for radial diffusion.

$$J = D\frac{\partial c}{\partial r} \qquad [2.11]$$

Substituting Equation 2.11 into Equation 2.6, gives Equation 2.12 describing the current.

$$i = Z_m FAD\frac{\partial c}{\partial r} \qquad [2.12]$$

Assuming that ∂c and ∂r can be approximated as Δc and Δr, and Δr equals the pit radius, then one obtains Equation 2.13 after substituting $A = 2\pi r^2$ for the surface area of the hemisphere.

$$i = 2\pi r Z_m FD\Delta c \qquad [2.13]$$

Equating 2.5 and 2.13 gives Equation 2.14, which is integrated to give Equation 2.15.

$$\frac{dr^3}{r} = 3V_m D\Delta c dt \qquad [2.14]$$

$$r = \sqrt{2V_m D\Delta c t} \qquad [2.15]$$

Finally substituting Equation 2.15 into Equation 2.13 gives Equation 2.16, which describes the variation of pit current with time.

$$i = 2\pi Z_m F(D\Delta c)^{3/2}\sqrt{2V_m t} \qquad [2.16]$$

The pit current for case 2 should increase with $t^{1/2}$ while according to Equation 2.15, *dr/dt* should decrease in time according to $t^{-1/2}$. If Equation 2.13 is divided by the pit surface area, the pit current *density* should decrease according to *1/r*. Geometries for the two cases are shown in Figure 2-6 with arrows showing the limiting flux of species away from the pit.

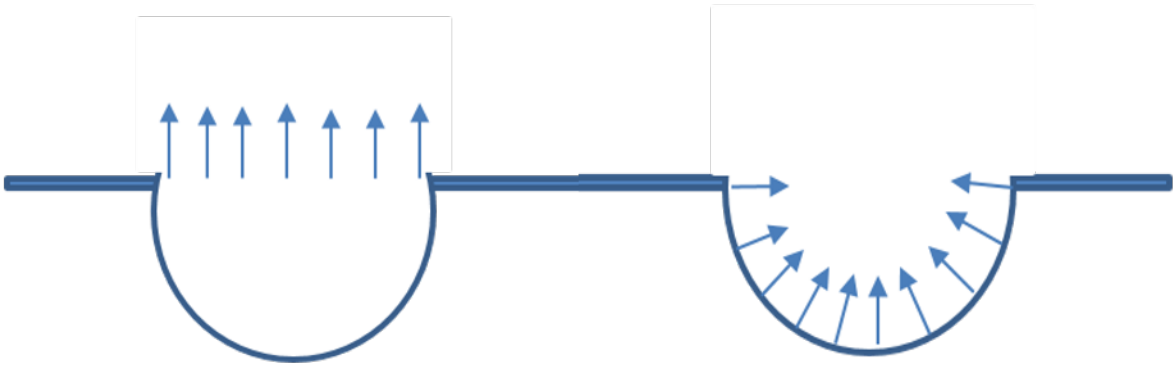

Figure 2-6: Case 1 (left) where flux is constant and pit current increases with the surface area of the pit opening. Case 2 (right) where flux varies according to Fick's 1st law.

2.4.2 Metastable Pits

It is generally agreed that all pits, regardless of whether they will attain stability or repassivate begin in the metastable state. It is thus appropriate to discuss all early pit growth in terms of metastability. Pit growth has three possible rate limiting phenomena; charge-transfer resistance, ohmic resistance and diffusion. Charge-transfer resistance is generally not considered rate-limiting because charge-transfer limited currents should give pit current densities (10^3-10^6 A cm^{-2}) that are orders of magnitude higher than any experimentally measured pit current density.[37] By the time the pit current becomes measurable beyond background noise, pit growth is limited by either ohmic resistance, diffusion or a combination of these phenomena.

Soltis recently separated metastable current transients into two types commonly reported in the literature.[2] Type I is characterized by a relatively slow increase of pitting current followed by a sudden current decrease signaling repassivation of the pit. Type II is characterized by a sudden spike of current followed by a slow decay and eventual repassivation of the pit. Type I transients are characteristic of pits measured in stainless steels while Type II are generally

associated with pits in more corrodible mild steels.[2] For pitting in Ni, Type I transients should be expected due to its high corrosion resistance.

Current transients for Type I metastable pits on stainless steels in halide electrolytes have been found to increase in time with $t^{1/2}$, t and t^2 dependencies.[38,39] As described in the previous section, the diffusion-controlled pit current from an open hemisphere should correspond to a current that increases with $t^{1/2}$. To obtain a current that increases with t^2, one must consider the flux to be limited at the pit mouth. This limitation is provided by a pit cover, that may be merely remnants of the oxide layer but also may contain undercut metal.[40-43] While the mathematical treatment in the previous section considered the pit under diffusion control, the same current dependencies are expected when the pit cover is considered an ohmic resistance.[40,41,44] A pit cover is now commonly accepted throughout the literature to be present, and necessary in the metastable stages of pit growth.

2.4.3 Pit Covers

Frankel et al found that for metastable pits in stainless steel, current increased with t^2 for early times and pit current density increased with potential.[40] They supposed that a pit cover limits (and also stabilizes) growth by providing a large resistance between the anode and cathode reactions. Growth was thought to take place in the absence of a salt film and repassivation resulted from rupture of the pit cover and loss of its resistance.[45] In their model, each pore in the pit cover was modeled as a resistor connected in parallel. Using the properties of a model circuit, they predicted a constant pit current density and transient that increased with t^2.[40] This situation is analogous to the diffusion model presented in Case 1 because in both cases the pit current is proportional to the pit mouth (ie area of the pit cover).

Similarly Vetter and Strehblow discussed the importance of a highly resistive pit cover in stabilizing a small corroding pit.[46] They calculated the time for salt film precipitation in a hemispherical pit with a current transient that varied according to t^2. By comparing predicted values with the lifetimes of metastable pits they concluded that metastable pits lost their resistive cover before precipitation of a salt film. Pits that became stable lost their cover after salt film precipitation and were stabilized by thickening of the salt film to compensate for the lost resistance of the pit cover.[47]

Pistorius and Burstein argued that metastable pits in stainless steel showing t^2 transients are under diffusion control.[41] They considered the pit cover to be a diffusion barrier that produced the diffusion geometry described by Case 1. Diffusion-limited growth was illustrated by initiating a cathodic scan while monitoring the transient of a metastable pit. They found that the current continued to increase with t^2 for some time after the start of the scan. Furthermore, transients that corresponded to cathodic scans were indistinguishable from those when a scan was not initiated. For a pit growing under ohmic control, a change in growth rate would be expected to coincide with the cathodic scan. The fine structure of the transient consisted of step-like increases that together generated a current that increased with t^2 for the first few seconds of growth. Step-like increases were attributed to the forming of perforations in the pit cover that effectively increased the flux from the pit in a step-like manner. A sharp increase in current was noted immediately prior to repassivation and was attributed to a sudden increase in flux from the pit caused by the partial or complete loss of the pit cover.[41]

2.4.4 Stability Criterion

As a consequence of metal dissolution, an enrichment of corrosion products in and near a corroding pit is expected. Several groups have studied pits that became stable and identified essentially the same criterion for stable pitting based on the idea that a minimum concentration of corrosion products is required to prevent repassivation. Williams et al established a stability criterion for pits in stainless steel based on the ratio of pit current to pit radius being greater than some critical value.[39] Pits that eventually repassivated did not attain this critical value. This criterion was satisfactorily extended to other metals and alloys.[41,42,48]

Galvele used a unidirectional pit and diffusion model to simulate the composition of pit electrolyte as a function of a critical quantity, the product of pit current density and pit depth.[30] Initially the focus was on maintaining a critically low pH at the pit bottom from the hydrolysis of corrosion products. Later the scope of this model was expanded to include subsequent hydrolysis reactions, buffering species and the accumulation of aggressive anions such as Cl^-. The full treatment showed that an increase in Cl^- concentration is coincident with pit acidification, and contributes to the aggressive environment that maintains pit propagation.[49]

Pistorius and Burstein calculated the stability product as the product of the pit current density and radius for a hemispherical pit to examine pit stability in stainless steel.[41] After

analysis of more than 200 metastable pit transients they concluded that the stability product did not exceed 0.3 A m^{-1} during the pit lifetime. While all pits grew initially in the metastable state (ie stability product < 0.3 A m^{-1}) those that attained stability reached the critical value. The critical value of the stability product corresponded to a concentration of around 75% of saturation value for the metal halide at the pit surface. At the critical value a plateau was observed where the stability product attained a constant value. The plateau signals a change in growth rate from t^2 to $t^{1/2}$. Since the rate change signals a change in rate-determining diffusion geometry, in this view it is coincident with the transition to stability.

Locally concentrated pit electrolytes have been simulated experimentally by preparing electrolytes having a low pH and high concentrations of metal halides. For stainless steels about 80% of the saturation value of metal ions was necessary to observe a direct transition from active dissolution to diffusion limited dissolution.[50] This value is close to that calculated by Pistorius and Burstein for the critical concentration.[41] Similarily other research has shown that to maintain active state dissolution on a salt free metal surface for a unidirectional artificial pit electrode, a concentration of more than 60% of the saturation value in metal ions is required.[51]

2.4.5 Salt Films

For a pit with sufficiently high pit current density, precipitation of a salt film is expected at short times. Alkire and Beck calculated that most corrosion systems, if exhibiting Tafel-like currents at the moment of nucleation, should precipitate a salt film in less than 1 ms.[37] Beck also considered two current densities, a diffusion current density and an ohmic current density. The ohmic current density is dictated by the applied potential and all resistances between the anodic and cathodic sites, while the diffusion current density is dictated by diffusion of corrosion products away from the corroding pit surface. Whenever the ohmic current density is greater than the diffusion current density a salt film should form.[52] Once the salt film forms, the two currents are regulated by the thickness of the film such that they balance and the film achieves a pseudo-steady-state thickness that increases only slightly as the pit grows larger.[46]

The structure of precipitated salt films has been proposed to consist of merely a thin layer of metal halide salt,[53] while others have proposed a bilayer structure in which a poreless layer is covered by a porous layer.[46,54,55] For dissolution of a Ni electrode in solutions containing a high concentration of Ni^{2+} and Cl^-, a bilayer structure was proposed where a thin pore-less inner layer

is formed initially and followed by the formation of a thick porous outer layer.[54] A similar bilayer has also been supposed when the electrolyte contains SO_4^{2-} and in this case the structure probably consists of a thin inner layer of $NiCl_2$ with a thick outer layer of porous $NiSO_4$.[55]

For galvanostatic experiments using Ni electrodes in solutions of high Cl^- content, Sand's equation, Equation 2.17, which predicts increase in concentration of corrosion products with time, was applied satisfactorily to the results.[54] One such experiment is shown in Figure 2-7 for a pit current density of 1.5 A cm^{-2} in an electrolyte saturated in $NiCl_2$. Dissolution at $t < 0.5$ s occurred through a thin $NiCl_2$ layer that was initially on the surface. At $t = 0.5$ s, a large increase in potential was measured due to the sudden appearance of a large resistance, which was taken to be the precipitation of a porous $NiCl_2$ layer from supersaturated pit solution. After the porous layer precipitated the potential continued to rise due to thickening of the porous layer which further increased the pore resistance. Examination of resulting electrode surface found it to be electropolished, consistent with metal dissolution through a thick salt film.[54]

$$i\sqrt{t} = \frac{Z_m F \Delta c \sqrt{\pi D}}{2} \qquad [2.17]$$

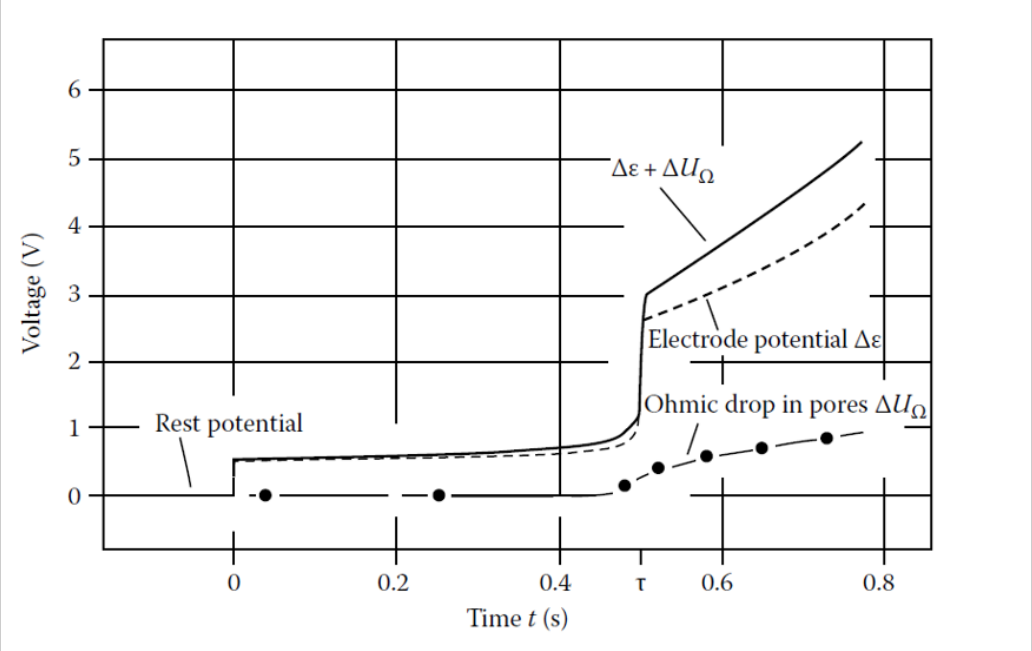

Figure 2-7: Voltage transient for Ni dissolution in saturated $NiCl_2$ solution with $i_p = 1.5$ A cm^{-2}. The potential increases are due to porous $NiCl_2$ film precipitation ($t = 0.5$ s) and porous film growth ($t > 0.5$ s). Reprinted from reference 54 with permission from Elsevier.

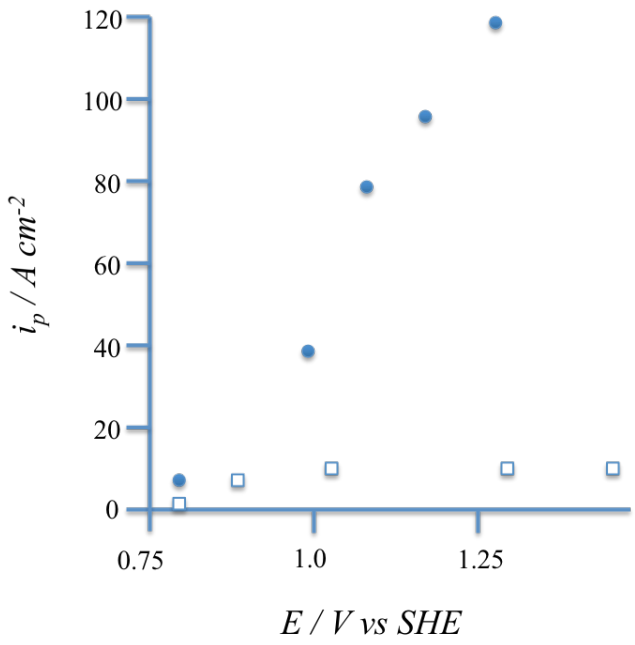

Figure 2-8: Pit current density as a function of potential for $E > E_p$. Closed circles indicate Ni in 0.1 M KCl electrolyte while open squares indicate Ni in 0.1 M KCl + 0.1 M K_2SO_4. Adapted from reference 55.

A large decrease in the maximum pit current density has been reported for Ni in the presence of non-aggressive anions such as SO_4^{2-} as illustrated in Figure 2-8. Pit current densities increased with increasing potential to more than 100 A cm^{-2} when the electrolyte was 0.1 M KCl, while they plateaued at less than 10 A cm^{-2} when the electrolyte was 0.1 M KCl and 0.1 M K_2SO_4. Apparently the presence of a porous $NiSO_4$ salt layer limits the pit current density to much lower values, while a porous $NiCl_2$ salt layer does not.[1,55] The maximum pit current density for Ni in Watts' electrolyte should be similar to the value of 10 A cm^{-2} due to the high concentration of SO_4^{2-}. The implication of this work for Ni in Watts' electrolyte is that increasing the potential significantly above the pitting potential should not significantly affect the pit current density.

2.4.6 Potential Drops

Potential drops occur within corroding pits due to electrolyte resistance, accumulation of corrosion products, pit acidification and the resistance across salt films. The potential drop across a precipitated salt film was addressed in the previous section and is depicted in Figure 2-7. The potential drop due to electrolyte resistance has been illustrated by Wang et al using artificially pitted Ni electrodes in H_2SO_4 solution.[56] They used an artificial pit with a depth of 7 mm and observed the potential drop along its depth. The drop within the pit electrolyte was large enough to observe an active-to-passive transition inside of the pit, which led to active corrosion at the bottom of the pit while the upper walls and pit opening remained passive. In sufficiently conductive electrolytes, the potential drop within a pit of micron dimensions due to solution resistance is predicted to be less than 1 mV and such a mechanism should only be observed for a large pit.[1]

In contrast, for a pit of micrometer dimensions, the potential drop within the pit due to the enrichment of corrosion products can be several tens of millivolts. As the pit environment becomes enriched in metal ions the potential drop, ΔU will vary according to Equation 2.18 where Δc is the increase in concentration of metal ion, Z_m is the charge on the metal ion, Z_j is the charge on species j, $c_{j,b}$ is the bulk concentration of species j, F is Faradays constant, R is the gas constant, and T is the absolute temperature. Figure 2-9 illustrates the effect of enrichment of Ni^{2+} as a function of ohmic drop for three electrolytes as calculated using Equation 2.18. In the presence of equal concentration of Cl- and SO_4^{2-} the potential drop is limited to about 50 mV or less. A drop 50 mV is sufficient to affect the growth if the applied potential is near a transition region in the anodic polarization curve.

$$\Delta c = -\frac{1}{Z_m}\sum_j z_j c_{j,b} e^{\frac{-z_j F}{RT}\Delta U} \qquad [2.18]$$

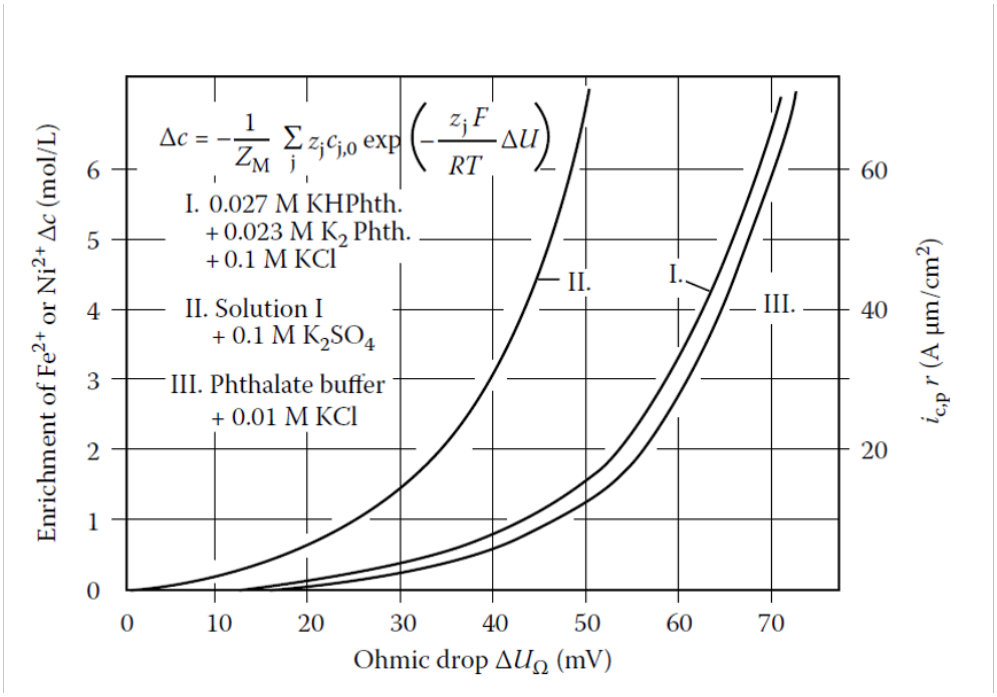

Figure 2-9: Potential drop due to the enrichment of Ni^{2+} inside of a corrosion pit. Enrichment of Ni^{2+} is directly proportional to the pit stability product. Migration of phthalate buffer used to maintain pH = 5 is also included in the calculation. Reprinted from reference 19 with permission from John Wiley & Sons.

A decrease in pH due to the hydrolysis of metal ions according to reaction 2.4 can also lead to a potential drop within a pit according to Equation 2.19 where pH_p and pH_b are the pit and bulk pH respectively. When only a single hydrolysis step is considered, the concentration of H^+ is given by Equation 2.20. The hydrolysis constant K_h for Ni^{2+} is on the order of 10^{-10} M and the minimum pH, which is limited by the solubility of the Ni^{2+} salts, is expected to be around 4.3 for a saturated solution of $NiCl_2$. When a saturation concentration of $NiSO_4$ is used the minimum pH is expected to be around 4.8. Thus the magnitude of the potential drop due to acidification is entirely dependent on the bulk solution pH. For the case of Ni in acidic electrolytes, and a single hydrolysis step, pit acidification should be minimal.

$$Ni^{2+}_{(aq)} + H_2O \rightleftharpoons Ni(OH)^+_{(aq)} + H^+_{(aq)} \qquad (2.4)$$

$$\Delta U = 0.059(pH_p - pH_b) \quad [2.19]$$

$$K_h = \frac{[NiOH^+][H^+]}{[Ni^{2+}]} \quad [2.20]$$

2.4.7 Pit Morphology

Two distinct pit morphologies have been reported in the literature for pits in Fe and stainless steels; crystallographic etch and polishing pits. Crystallographic etch pits have a shape dictated by crystallographic facets, while polishing pits are hemispherical with an electropolished interior. Schwenk found a potential dependence on pit morphology for pits formed on stainless steels. At low applied potentials pits were crystallographically faceted while at higher potentials they were hemispherical with a circular pit mouth and generally had a polished interior although some hemispherical pits had dull interiors.[57] Pickering and Frankenthal showed hemispherical and crystallographic pits were possible at high potentials and noted that larger pits had interiors that were always electropolished.[58] Sato et al noted that for stainless steel, crystallographic pits formed at lower potentials, giving lower currents, while polishing pits formed at higher potentials and had higher pit current densities.[59,60] In this case the transition from crystallographic to polished pits was near the critical concentration of corrosion products for pit propagation in stainless steel. According to this view, crystallographic etch pits lacked sufficiently high current density to precipitate a salt film, however they maintained a pit environment above the critical concentration. They also noted that when pits were initiated at potentials above E_p they grew as polished pits. However, if the potential was lowered, the pit either repassivated or in some cases continued to propagate crystallographically with deep irregular pitting into the metal.[60]

There has been some work that considers that crystallographic etch pits can grow under a salt film provided the film is thin, on the order of 10 nm.[46,52]At higher current densities a thicker salt film should form giving the pit an electropolished appearance due the presence of additional salt layer that could grow to several hundreds of nanometers. In particular for Fe, the presence of a 5 nm film of $FeCl_2$ was noted for crystallographic etch pits while for an electrolyte containing an excess of SO_4^{2-}, a thick salt film was formed and pits were electropolished.[61]

2.4.8 Lacy Pit Covers

The presence of lace-like pit covers for pits in stainless steel, Fe and Ni has been well documented and one such example is shown in Figure 2-10 a).[56,62-65] These pit covers are visible optically and may be considered inherently different from covers that may be merely remnants of the initial oxide layer because they contain undercut metal, making them more robust. Most pits that grow beneath a lacy pit cover show $t^{1/2}$ growth, corresponding to that of an open hemisphere, indicating that the pit cover does not limit the growth. Several mechanisms have been proposed for their occurrence. Harb and Alkire found that local environments of enriched corrosion products found *outside* of the pit extend to distances many times the pit radius.[66] As a result, local pH and potential drops should also be expected in this region. These effects have been shown to increase the frequency of pit nucleation in the vicinity of a corroding pit, known as secondary nucleation.[67] In this way pitting should be correlated spatially and temporally around a central corrosion pit and a circular pattern of pits should be expected creating a lace-like appearance. However, it is unclear how a pattern of individual pits can become connected to a central hemisphere without metal undercutting. Other explanations of lacy pit cover formation are based on metal undercutting due to the solution chemistry *inside* of the pit.

Wang et al proposed that potential drops lead to flask-shaped pits that eventually grow back toward the surface creating the appearance of a lace-like pattern around the pit opening.[56] This mechanism requires that different regions of the pit be subject to large differences in corrosion rates due to potential drops. For a small pit in Ni in Watts' electrolyte, the potential drop within the pit due to enrichment of corrosion products is at most 0.05 V with negligible contribution from solution resistance and pit acidification. This mechanism should only lead to metal undercutting for a small pit if the applied potential is near the active-passive transition.[1]

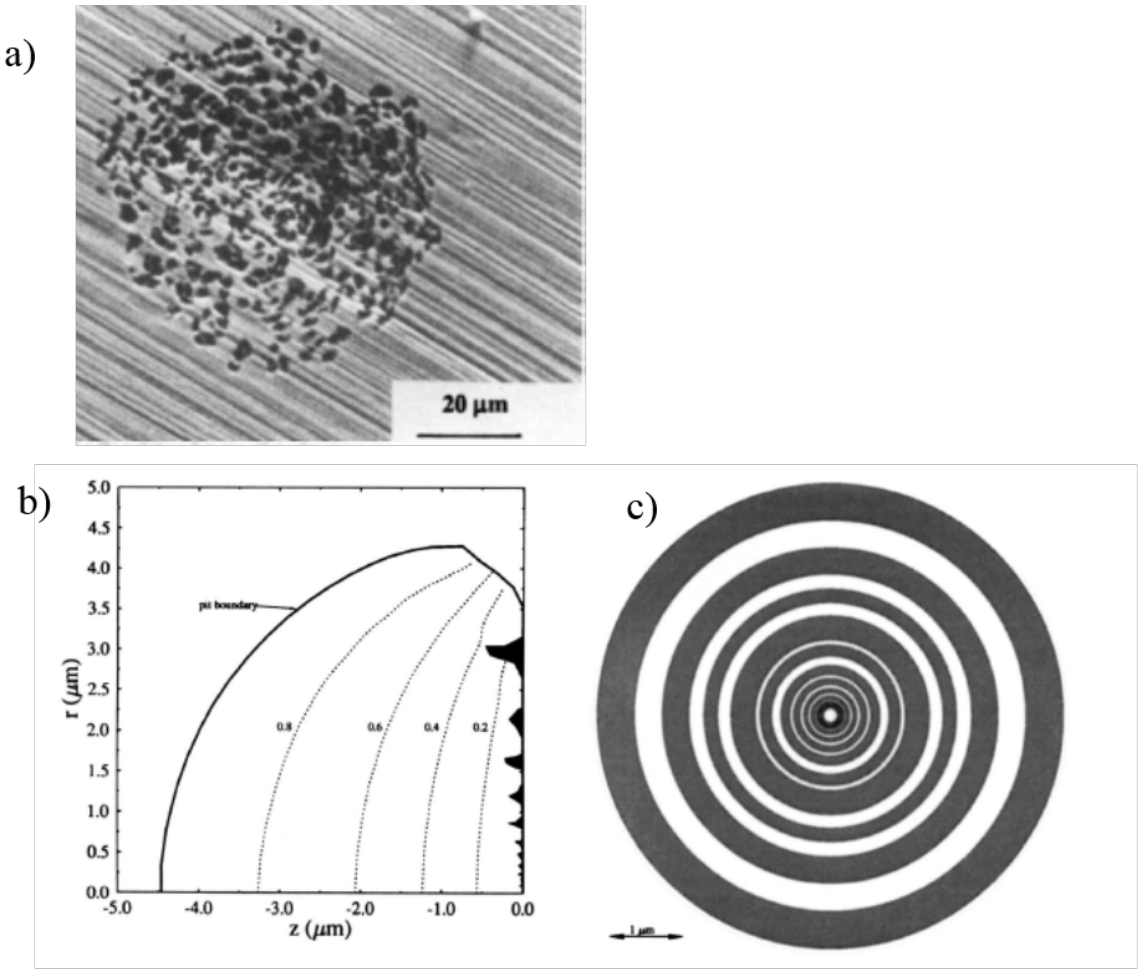

Figure 2-10: SEM image of lacy pit cover in stainless steel a). Lacy cover formation predicted by diffusional model showing a pit cross section with metal islands b), and metal islands predicted in concentric rings that cover the pit mouth c). Reprinted with permission from reference 63. Copyright 1998, The Electrochemical Society

The appearance of lacy pit covers for small pits in Ni is probably best explained by considering that the concentration of corrosion products dictates the corrosion rate, producing differential rates within the pit. This was first described by Ernest et al[62] and later computationally modeled by Laycock et al.[63] They developed a computational simulation that produced undercut hemispheres with lace-like covers for a pit growing under diffusion control. Their simulation considered that nucleation produced an open hemisphere with a radius of 100 nm that was covered in a thin salt film. The corrosion current at any point in the hemisphere was proportional to the concentration of corrosion products, with the overall current given by Equation 2.13. Wherever the concentration dropped below the critical concentration, dissolution

current was zero (ie repassivation). During the simulation the concentration of corrosion products at the pit mouth quickly dropped below the critical concentration and undercutting began. As the pit interior continued to grow, it severely undercut the bulk metal and eventually grew back toward the electrode surface causing perforations in the pit cover. As this repeated several times, it produced a series of concentric radii of metal islands depicted in Figure 2-10 b) and c). The calculated current transient for the simulation showed a baseline current that scaled roughly with $t^{1/2}$ and contained a series of current spikes followed by slow decay periods due to the cycle of undercutting and perforation. Increasing the value of the critical concentration led to slower growth and much larger metal islands. When the zero-concentration boundary was extended an infinite distance from the electrode surface, the same undercutting behavior was observed but the onset was delayed. According to this work, for a corrosion system with a critical concentration significantly higher than the bulk concentration, metal undercutting should always be expected.

2.4.9 Repassivation

The Einstein-Smoluchowski relation for the diffusion of a species from a spherical pit of radius r has been used to calculate the repassivation time, t_r using Equation 2.21 based on the assumption that diffusion of corrosion products out of the pit is the rate-determining step of repassivation. At constant pit current density, the radius can be calculated using Faradays law and it is apparent that the repassivation time should depend on the square of the pitting time, t_p.[1] Measurements of the repassivation time for Ni electrodes in Cl^- electrolytes have shown that the repassivation time is explained satisfactorily by combining Equations 2.21 and 2.22.[68] Thus the diffusion of corrosion products out of the pit should be considered the rate-determining step for repassivation.

$$t_r = \frac{r^2}{2D} \qquad [2.21]$$

$$r = \frac{i_p t_p V_m}{Z_m F} \qquad [2.22]$$

2.4.10 Effect of Temperature

For corrodible metals and alloys there exists a critical pitting temperature (CPT), below which stable pitting is not possible at a potential cathodic of transpassive dissolution. In other words, as temperature surpasses the critical temperature, the pitting potential decreases sharply to a potential below the onset of transpassive dissolution.[69] Above the CPT, the pitting potential usually shows a weak or even negligible dependence on temperature. An explanation for the existence of the critical pitting temperature is based on the competition between Cl^- adsorption and oxide formation. At temperatures below the CPT, the formation of a thin Cl^- layer directly on the metal surface is not possible and oxide will always preferentially form in the event of bare metal exposed to electrolyte.[70,71]The CPT for Ni in Watts' electrolyte is below ambient temperatures and the pitting potential should be considered nearly independent of temperature as it is increased above ambient temperature.

Increasing the temperature above room temperature has two significant effects on the pitting of Ni in Cl^- electrolyte. An increase in the diffusion coefficient is expected along with an increase in solubility of $NiSO_4$ and $NiCl_2$. The solubility of $NiSO_4$ $6H_2O$ and $NiCl_2$ $6H_2O$ are 1.4 M and 2.6 M at 20 ^oC and 2.1 M and 3.4 M at 60 ^oC respectively.[72] Higher current densities will be attainable at elevated temperatures prior to precipitation of a salt film. As well, the rate limiting current dictated by a porous $NiSO_4$ salt film should increase as temperature increase owing to the increased diffusion coefficient. While specific data for the variation of the diffusion coefficient for Ni^{2+} in $NiCl_2$ or $NiSO_4$ solutions with temperature could not be found, data for Fe^{2+} has been approximated.[69] The approximate diffusion coefficient for Fe^{2+} in a solution of $FeCl_2$ was 0.86×10^{-5} cm^2 s^{-1} at 25 ^oC and 1.64×10^{-5} cm^2 s^{-1} at 55 ^oC. A similar increase should be expected for Ni^{2+}.

2.5 References

[1] Strehblow, H-H.; Marcus, P. Mechanisms of Pitting Corrosion. In *Corrosion Mechanisms in Theory and Practice*; Marcus, P., Ed.; CRC Press, Boca Raton, USA, 2011; pp 349-393.

[2] Soltis, J. *Corrosion Science,* **2015,** *90*, 5.

[3] Payne, B. P.; Grosvenor, A. P.; Biesinger, M. C.; Kobe, B. A.; & McIntyre, S. A. *Surface and Interface Analysis,* **2007**, *39*, 582.

[4] Cabrera, N.; Mott, N. F. *Rep. Prog. Phys*. **1948-1949**, *12*, 163.

[5] Payne, B.P.; Biesinger, M.C.; McIntyre, N.S. *Journal of Electron Spectroscopy and Related Phenomena* **2009**, *175*, 55.

[6] Pourbaix, M. *Atlas of the Electrochemical Equilibria in Aqueous Solutions*; Pergamon: Oxford, 1966.

[7] Barbosa, M.R.; Bastos, J.A.; Garcia-Jareno, J. J.; Vicente, F. *Electrochimica Acta* **1998**, 44, 957.

[8] Zuili, D.; Maurice, V.; Marcus, P. *J. Electrochem. Soc.* **2000**, *147*, 1393.

[9]Hoppe, H-W.; Strehblow, H-H. *Surf. Interf. Anal.* **1989**, *14*, 121.

[10] Hoppe, H-W.; Strehblow, H-H. *Corrosion Science,* **1990**, 31, 167.

[11] Marcus, P.; Herbelin, J-M. *Corrosion Science* **1993,** *34*, 1123.

[12]Magnussen, O. M.; Scherer, J.; Ocko, B. M.; Behm, R.J.; *J. Phys. Chem. B* **2000,** *104*, 1222.

[13] Suzuki, T.; Yamada, T.; Itaya, K. *J. Phys. Chem.* **1996,** *100*, 8954.

[14] Michell, D. F.; Sproule, G. I.; Graham, M. J.; *Appl. Surf. Sci.,* **1985,** *21*, 199.

[15] Marcus, P. In *Electrochemistry of Well-Defined Surfaces,* Eds. Oudar, J.; Marcus, P.; Clavilier, J. Special Volume of *J. Chim. Phys.* **1991,** *88*, 1697.

[16] Kolotyrkin, Y. M. *Corrosion,* **1963,** *19*, 261.

[17] Hoar, T. P.; Jacob, W. R. *Nature,* **1967,** *216*, 1299.

[18] Benamar, S. Thesis, Universite Pierre et Marie Curie, Paris, France, 1998.

[19] Strehblow, H-H. *Werkst. Korros.,* **1984,** *35*, 437.

[20] Seo, M.; Matsumura, Y.; Sato, N. In *Proc. 8th Int. Cong. Met. Corros DECHEMA, Frankfurt am Main.* **1981,** pp 108.

[21] Bardwell, J. A.; Macdougall, B. *Electrochim. Acta* **1989**, *34*, 229.

[22] Bardwell, J.A.; Macdougall, B. *J. Electrochem. Soc*. **1988**, *135*, 2157.

[23] Hoar, T. P.; Mears, D. C.; Rothwell, G. P. *Corros. Sci.* **1965**, *5*, 279.

[24] Evans, U. R.; *J. Chem. Soc*. **1927**, 1020.

[25] Chao, C. Y.; Lin, L. F.; Macdonald, D. D. *J. Electrochem. Soc.* **1981**, *128*, 1187.

[26] Ahn, S.; Kwon, H.; Macdonald, D. D. *J. Electrochem. Soc*. **2005**, *152*, B482-B490.

[27] Lu, P.; Engelhardt, G. L.; Kursten, B.; Macdonald, D. D. *J. Electrochem. Soc*. **2016**, *165*, C156.

[28] Lochel, B. P.; Strehblow, H-H. *Werkst. Korros*. **1980**, *31*, 353.

[29] Evans, U.R.; *Corrosion and Oxidation of Metals*; Edwards Arnold: London, 1960.

[30] Galvele, J. R. *J. Electrochem. Soc.* **1976**, *123*, 464.

[31] Burstein, G. T.; Mattin, S. *Philosophical Magazine Letters* **1992,** *66*, 127.

[32] Burstein, G. T.; Liu, C.; Moloney, J. J.; Vines, S. P. *Corros. Mater.* **2009**, *34*, 26.

[33] Riley, A.M.; Wells, D.B.; Williams, D.E. *Corros. Sci*. **1991**, 32, 1307.

[34] Hoar, T.P.; *Corros. Sci*. **1967**, 7, 341.

[35] Sato, N. *Electrochim. Acta*, **1971**, 16, 1683.

[36] Burstein, G. T.; Mattin, S. P. The nucleation and early stages of growth of corrosion pits. In *Critical Factors in Localized Corrosion II;* Natishan, P. M.; Kelly, R. G.; Frankel, G.S.; Newman, R.C. Eds.; The Electrochemical Society: Pennington, 1996, pp 1-14.

[37] Beck, T. R.; Alkire, R. C. *J. Electrochem. Soc.* **1979**, *126*, 1662.

[38] Williams, D. E.; Stewart, J.; Balkwill, P. H. In *Critical Factors in Localized Corrosion;* Frankel, G.S.; Newman, R.C. Eds.; The Electrochemical Society, Pennington, 1992; pp 36-44.

[39] Ezuber, H.; Newman, R.C. In *Critical Factors in Localized Corrosion;* Frankel, G. S.; Newman, R. C. Eds.; The Electrochemical Society: Pennington, 1992; pp 120-127.

[40] Frankel, G. S.; Stockert, F.; Hunkeler, F.; Boehni, H. *Corrosion* **1987**, *43*, 429.

[41] Pistorius, P. C.; Burstein, G. T. *Philos. Trans. R. Soc. London A* **1992**, *341*, 531.

[42] Williams, D. E.; Stewart, J.; Balkwill, P. H. *Corrosion Science* **1994**, *36*, 1213.

[43] Newman, R. C.; Franz, E. M. *Corrosion* **1984**, *40*, 325.

[44] Alkire, R. C.; Wong, K. P. *Corrosion Science* **1988**, *28*, 411.

[45] Frankel, G.S. Localized corrosion of metals: a review of the rate-controlling factors in initiation and growth. In *Passivity of Metals and Semiconductors*; Ives, M. B.; Luo, J. L.; Rodda, J.R. Eds.; The Electrochemical Society, Pennington, 2001; pp 445-477.

[46] Vetter, K.J.; Strehblow, H-H. In *Localized Corrosion*; Steahle, R.W.; Brown, F.; Kruger, J.; Agrawal, A. Eds.; NACE International: Houston, 1974; pp. 240-251.

[47] Moayed, M. H.; Newman, R.C. *Corrosion Science* **2006**, *48*, 1004-1018.

[48] Pride, S.T.; Scully, J.R.; Hudson, J.L. *J. Electrochem. Soc,* **1994**, *141*, 3028.

[49] Galvele, J.R. *Corrosion Science* **1981**, *21*, 551.

[50] Mankowski, J.; Szklarska-Smialowska, Z. *Corrosion Science*, **1975**, 15, 493.

[51] Newman, R.C.; Isaacs, H.S. *J. Electrochem. Soc*. **1983**, *130*, 1621.

[52] Beck, T.R. In *Advances in Localized Corrosion*; Isaacs, H.S.; Bertocci, U.; Kruger, J.; Smialowska, S. Eds.; NACE International: Houston, 1990; pp 85-87.

[53] Isaacs, H.I. *J. Electrochem. Soc.* **1973**, *120*, 1456.

[54] Strehblow, H-H.; Wenners, J. *Electrochim. Acta* **1977**, *22*, 421-427.

[55] Strehblow, H-H. *Habilitationsschrift,* Freie Universitat, Berlin, 1977.

[56]Wang, M.; Pickering, H.W.; Xu, Y. *J. Electrochem. Soc*., **1995**, *142*, 2986.

[57] Schwenk, W. *Corrosion* **1964**, *20*, 129-137.

[58] Pickering, H.W.; Frankenthal, R.P. *J Electrochem. Soc.* **1972**, *119*, 1297.

[59] Sato, N. In *Corrosion and Corrosion Protection*; Frankenthal, R.P.; Mansfeld, F. Eds.; The Electrochemical Society: Pennington, 1981; pp 110-122.

[60] Sato, N. *Corrosion Science* **1995**, *37*, 1947-1967.

[61] Strehblow, H-H.; Vetter, K.J.; Willgallis, A. *Ber. Bunsen. Ges. Phys. Chem.* **1971**, *75*, 823.

[62] Ernest, P.; Laycock, N.J.; Moayed, M.H.; Newman, R.C. *Corros. Sci.* **1997**, *39*, 1133.

[63] Laycock, N.J.; White, S.P.; Noh, J.S.; Wilson, P.T.; Newman, R.C. *J. Electrochem. Soc.* **1998**, *145*, 1101.

[64] Barlow, B.C.; Szymanski, G.; Lipkowski, J.; Shobeir, B.; Love, B.; Burgess, I.J. *J. Electrochem. Soc.* **2016**, C164-C170.

[65] Heurtault, S.; Robin, R.; Rouillard, F.; Vivier, V. *Electrochim. Acta* **2016**, *203*, 316-325.

[66] Harb, J.N.; Alkire, R.C. *J. Electrochem. Soc*. **1991**, *138*, 3568.

[67] Frankel, G.S. *J. Electrochem. Soc.* **1998**, *145*, 2186.

[68] Strehblow, H-H. *Werkst. Korros.* **1976**, *27*, 792.

[69] Laycock, N.J.; Newman, R.C. *Corros. Sci.* **1998**, *40*, 887-902.

[70] Laycock, N.J.; Moayed, M.H.; Newman, R.C. *J. Electrochem. Soc.* 1998, *145*, 2622-2628.

[71] Salinas-Bravo, V.M.; Newman, R.C. *Corros. Sci.* **1994**, 20, 597.

[72] "Aqueous Solubility of Inorganic Compounds at Various Temperatures," In *CRC Handbook of Chemistry and Physics, 96th Edition* (Internet Version 2016), Haynes, W.M. Ed.; CRC Press/Taylor and Francis: Boca Raton, USA; 2016.

CHAPTER 3

Experimental Materials and Methods

3.1 Reagents and Solutions

Nickel sulfate hexahydrate (98%, Alfa Aesar), boric acid (99+%, Alfa Aesar), nickel chloride hexahydrate (98%, Alfa Aesar), dimethylglyoxime (> 99.0%, Sigma-Aldrich), nitric acid (ACS plus, Fisher Scientific) and sulfuric acid (ACS, Fisher Scientific) were purchased and used without further purification. All solutions and dilutions were prepared using ultra-pure Millipore water (> 18 MΩcm). For the preparation of Ni standards a concentrated stock solution was made by dissolving a known mass of Ni p-pellet in 15.8 M nitric acid and subsequently diluted with Millipore water. The concentrated stock solution ~10,000 mg L^{-1} was serially diluted to obtain standard solutions in the range of 0.1-100 mg L^{-1}.

For 85-hour electrodissolution experiments it was necessary to adjust the pH of the Watts' electrolyte several times during the course of the experiments. When the pH reached 4.5, 1 M H_2SO_4 solution was added dropwise to the Watts' electrolyte until the pH dropped to within 3.3-3.5.

3.2 Electrochemistry Materials

Anodes consisted of carbonyl Ni p-pellets supplied by Vale Canada. The p-pellets are spherical with a diameter of 8-12 mm and Ni content > 99.98% by weight. Anode pellets were soldered to an insulated wire, encased in a non-conductive epoxy and mechanically polished on abrasive papers (P 600, 1200, 2500). Anodes were then polished with successively smaller diamond suspensions (15 μm, 6 μm, 3 μm, 1 μm) on Micropad II polishing pads. For experiments requiring a highly polished electrode, final polishing was done using a Giga 0900 Vibratory Polisher purchased from Pace Technologies with 0.05 μm alumina slurry and a Tricote polishing pad. All polishing pads and polish were purchased from Pace Technologies. Following polishing steps, samples were rinsed with Millipore water and allowed to sit in air to

allow the air-formed oxide to develop. Auxiliary electrodes were fabricated from either Cu foil (McMaster Carr) or Ni wire (> 99.5%, Alfa Aesar).

3.3 Electrochemical Methods

3.3.1 General Methods

Several common electrochemical methods were utilized in this work, and these have been described extensively elsewhere.[1] For this reason, common methods themselves will not be discussed in detail. One method that involves pulsing the potential was specifically developed for this thesis and will be discussed in more detail below.

All electrochemical experiments were performed in Watts' electrolyte containing $NiSO_4$ $6H_2O$ (240 g L^{-1}), $NiCl_2$ $6H_2O$ (20 g L^{-1}), H_3BO_3 (20 g L^{-1}) at room temperature (22 +/- 1 ^oC) except where noted. A standard three-electrode cell was used with a Ni p-pellet working electrode, Ni-wire reference and an auxiliary electrode. Potentials are referenced to a Ni wire in Watts' electrolyte so that the reported potential is, by definition, the polarization. The auxiliary electrode was a sheet of Cu foil except for the *in situ* optical cell, which had a Ni wire auxiliary electrode. All reported current densities were calculated using the geometric area of the Ni working electrode as measured with an optical microscope. All experimental methods were carried out using software written in the LabView programming environment and a DAQ board from National Instruments, except where noted. Unless otherwise specified, electrochemical experiments were carried out using a PAR Model 173 Potentiostat/Galvanostat.

3.3.2 Current Transients

Current transients were collected on an Autolab PGSTAT302N using the chrono amperometry methods available in Nova 2.0.1. In general, the length of the transient depended on the potential so the sampling rate was adjusted for each potential so the number of data points was around 70,000. This corresponded to sampling rates of 0.1 ms for 1.0 V and 1.2 V, while a sampling rate of 2 ms was sufficient for the transient collected at 0.6 V.

3.3.3 Pulsed Potential Dissolution

To carry out the pulsed potential experiments, software was written using Labview. The execution of the software is summarized as follows. A square potential wave was generated using LabView and sent to the external input of the Solartron 1287 Electrochemical Interface. The current response was digitized with a sampling rate of 40 kHz and plotted in LabView. After each complete cycle of the potential wave, the current response was numerically integrated using Simpson's rule to give the charge for the cycle. By integrating the entire cycle, non-Faradaic currents associated with charging and discharging of the electrical double layer negated each other. In addition, any small amount of current corresponding to passive state Ni dissolution during the 0 V phase was also counted. The charge was cumulatively added at the end of each cycle to monitor the extent of dissolution. From this charge, the average current for the entire experiment was calculated after each cycle so that the duty cycle (fraction of time spent at the dissolving potential) could be adjusted in order to maintain a constant average current. For the Solartron 1287, a small current offset was needed to obtain a baseline current that was zero. The magnitude of this offset was determined by running the program for several minutes with the cell switched off prior to the start of the electrodissolution experiment. The charge-per-cycle offset value was then subtracted from each integrated cycle for the duration of the experiment.

3.4 Surface Analysis

3.4.1 In Situ Optical Microscopy

In situ optical microscopy was carried out using an Accu-Scope 3035 inverted metallurgical microscope with a custom designed cell. Images were captured using Micrometrics SE software using a time-lapse capture and an auto brightness feature to account for any changes in lamp brightness or surface reflectivity over the course of the experiment. The maximum capture rate of the software was 1 s but due to the duration of the experiments, images were usually captured at 60 s intervals. The synchronization of the electrochemical experiments and the time-lapse capture allowed for correlation between electrochemistry and changes in the anode surface. The *in situ* cell, shown in Figure 3-1, utilized a commercially available petri dish embedded with a #0 microscope coverslip (Matek, USA) as the main cell reservoir. For the electrode assembly, a custom made polyethylene disk was fitted with Ni pellet working

electrode, Ni wire auxiliary electrode and Ni wire reference electrode which were fixed with epoxy and polished according to the procedure described above. Double-sided tape was used as a spacer to provide an electrolyte channel of about 260 µm between the working electrode and the glass coverslip and also served to hold the electrode assembly in place within the petri dish. The cell reservoir was filled with approximately 10 ml of Watts' electrolyte, which given the size of the working electrode, was sufficient that the composition of the bulk electrolyte did not change significantly over the course of a dissolution experiment.

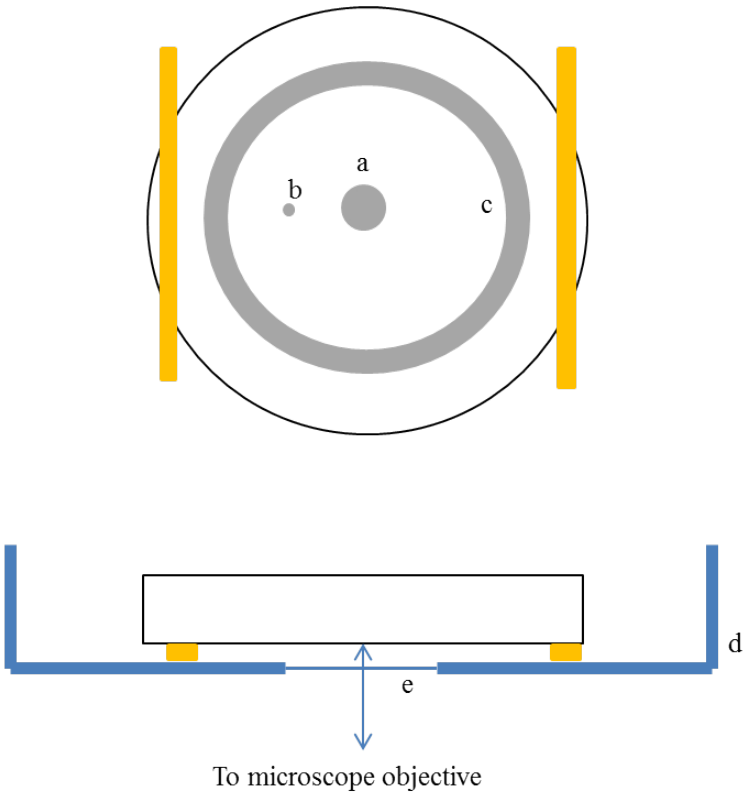

Figure 3-1: Diagram of *in situ* cell. Above view shows the face containing the working electrode a), reference electrode b), and auxiliary electrode, c), embedded in a polyethylene disk. Yellow indicates Kapton tape spacer to provide and electrolyte channel. Petri dish reservoir d), and glass coverslip window e), are indicated in the cross-sectional image of the assembled cell (lower). Double-headed arrow shows the incident and reflected light.

3.4.2 Scanning Electron Microscopy

All SEM images presented in this thesis, except those presented in Chapter 1, were collected on a Jeol 840A scanning electron microscope operating in high-vacuum mode with a beam energy of 15 keV. All images were collected using the secondary electron imaging mode (SEI).

3.4.3 White Light Interference Microscopy (WLIM)

WLIM is a non-contact surface profiling technique with sub-micron spatial resolution and the depth resolution of a few nanometers. Analysis of the images to obtain pit dimensions was done manually using Gwyddion image analysis software. After plane leveling and zero adjustment of each image, a threshold algorithm was applied to the image to identify the most prominent pits. Line profiles through the center of each pit were then extracted and the dimensions of each pit recorded. For each sample a minimum of 4 different images were analyzed, which were taken from different regions on the sample to ensure that the dimensions of the pits were representative of the entire sample.

3.5 Residue Quantification

3.5.1 Residue Collection

Anode assemblies were fabricated using four pellets so that a larger sample size could be used in each experiment. The pellets were soldered directly to a wire, epoxied and polished as described previously. The anode assembly was encased in a polypropylene mesh bag to capture anode residue throughout the experiment. Following the dissolution experiments, anode assemblies were rinsed serially within the anode bag so that any residue that washed free of the bulk was captured. The anode bag itself was then rinsed successively with Millipore water until the washings showed no detectible Ni^{2+} from residual electrolyte as determined by a nickel dimethylglyoxime spot test (see below). The anode bag and residue contents were then transferred to beaker containing 4 M HNO_3 solution for more than 120 minutes to dissolve the Ni residue. Upon removal from the acid solution, the bag was again rinsed serially and the Ni containing solution was transferred to a volumetric flask. This solution was used for determination of Ni by flame atomic absorption and dimethylglyoxime spot test.

3.5.2 Nickel Dimethylglyoxime Spot Test

A simple quantitative test for Ni^{2+} in aqueous solution was adapted from a literature procedure to quantify Ni residue.[2] The test was eventually replaced by flame atomic absorption (FAA) but a complete description of the method is provided herein as significant effort was made to develop the test and optimize its performance. Although FAA is a superior method for quantification, the colorimetric test was extremely useful due to its simplicity and ability to detect aqueous Ni^{2+} down to concentrations of 5 mg L^{-1} visually. The test is based on the highly coloured, water insoluble complex formed between Ni^{2+} and dimethylglyoxime. A saturated solution of dimethylglyoxime in 95% ethanol was applied to a piece of Basics brilliant 96, 20 weight, premium multipurpose office paper and allowed to dry. Several 3 µL aliquots of 0.1 M $NH_{3(aq)}$ were applied to the paper directly followed by 3 µl aliquots of the Ni^{2+} containing standards and unknowns. An approximation of the unknown Ni^{2+} concentration was possible by simple visual comparison but a digital colourimetric method was also developed. For the digital method the spotted paper was scanned as a 600 dpi colour image and sections containing each standard and unknown were cropped and saved as a separate bitmap image. Red, green, blue (RGB) analysis was carried out by first extracting the RGB values for each pixel in the image using free "get RGB" software.[3] The software returns a comma-separated values file with the total number of rows equal to the number of pixels in the image, and columns corresponding to R, G and B values. The RGB values give the contribution of each colour to the pixel. For example, a white pixel has R=255, G=255 and B=255, while a black pixel has R=0,G=0 and B=0. A red pixel has R=255, G=0, B=0. Due to the mostly red composition of the nickel dimethylglyoxime spot, the value 2R-(G+B) was used as a measure of the spot intensity. This ensured that white pixels had near-zero values and any noise pixels, which had much higher G and B contributions, had negative values. All pixels that had 2R-(G+B) values less than 1 were omitted from further calculations. The sum of 2R-(G+B) for all remaining pixels was used to make a calibration point for each standard, which produced a linear plot over the range 5-50 mg L^{-1}.

3.5.3 Flame Atomic Absorption

All concentrations of Ni^{2+} from residue were first determined by dimethylglyoxime spot test and then verified by flame atomic absorption (FAA). FAA experiments were carried out on a Perkin Elmer AAnalyst 400 using the 352.5 nm Ni line with a slit width of 0.5 nm. This line gives the most linear response over the concentration range of 1-100 mg L^{-1}. While this line is not the most sensitive, the response is less susceptible to non-atomic absorbance compared to other Ni lines and was sufficient for the concentrations of interest. The lamp current was 4 mA and the flame was an oxidizing acetylene/air mixture. Each standard and unknown were sampled 5 times. The reported error bars represent the standard deviation for the 4 repeat trials for each dissolution method and are not associated with FAA uncertainty.

3.6 References

[1] Bard A.J.; Faulkner, L.R. *Electrochemical Methods: Fundamentals and Applications*; Wiley, New York: 2001.

[2] Salman, M.; Shafique, U.; Waheed-uz-Zaman; Rehman, R.; Yousaf, A.; Azhar, F.; Anzano, J.M. *J. Mex. Chem. Soc.* **2011**, 55, 214-217.

[3] Get RGB. https://itg.beckman.illinois.edu/technology_development/solftware_development/get_rgb/ (accessed June 2015)

CHAPTER 4

Results and Discussion

Throughout this chapter, two different current densities will be discussed, the electrode current density and the pit current density. They are related but are quite different and should not be confused. The electrode current density is calculated using the total current and dividing by the geometric area of the electrode. The pit current density is the current from an individual pit divided by the surface area of the pit. Pit current densities are determined by measuring the current and size of a single pit (usually for a hemispherical shape) or by using a uni-directional lead-in-pencil type electrode where the pit surface area remains constant. Pit current densities were not measured in this thesis and all reported current densities correspond to electrode current densities, which will be indicated as j, and reported in units of A dm^{-2} as is the convention in electroplating. Whenever pit current densities are discussed in this chapter they will be clearly identified as pit current density and represented by i_p.

4.1 Linear Scan Voltammetry

Linear scan voltammetry was used to examine the regions of anodic dissolution of a Ni electrode in Watts' electrolyte at a scan rate of 1 mV s^{-1}. The regions of active, passive and pitting potentials are indicated in Figure 4-1 with red, green and blue regions respectively. The active region begins at low polarization and is confined to 0.0 V < E < +0.1 V. The maximum current density recorded in the active region in this region corresponds to 0.007 A dm^{-2} and occurs at E = 0.055 V. The inflection point in the active current signals the start of passivation around E = 0.060 V where passive film formation becomes kinetically dominant. As the passive layer forms, the current decreases until it reaches a minimum, at which point a complete passive film covers the surface. The passive region occurs from 0.1 V < E < 0.32 V and is identified by a very small current density 0.002 A dm^{-2} that corresponds primarily to passive dissolution. At E > 0.32 V the current density begins to rise above passive levels due to the formation of propagating pits and the pitting potential, E_p is taken to be 0.32 V. As the potential is scanned further positive, the pitting current begins to fluctuate, a phenomenon that has been attributed to

the formation of perforations in pit covers, or to the presence of electropolishing salt films on the pit interior.[1-5] After the scan direction is reversed at $E = 0.7$ V, the current continues to rise indicating that pit growth is diffusion controlled during this stage. Initially the current continues to increase at nearly the same rate, however the increase slows and eventually begins to decrease around $E = 0.550$ V in the cathodic scan. At this point the current fluctuations begin to subside, indicating no new perforations in pit covers or that the electropolishing salt film has been lost. The presence of a dissolution current in the cathodic scan at potentials below the pitting potential indicates the repassivation process is hindered by diffusion of corrosion products out of the pit. The surface is entirely repassivated around $E = 0.195$ V in the cathodic scan, approximately 0.125 V less than the potential required to initiate propagating pits.

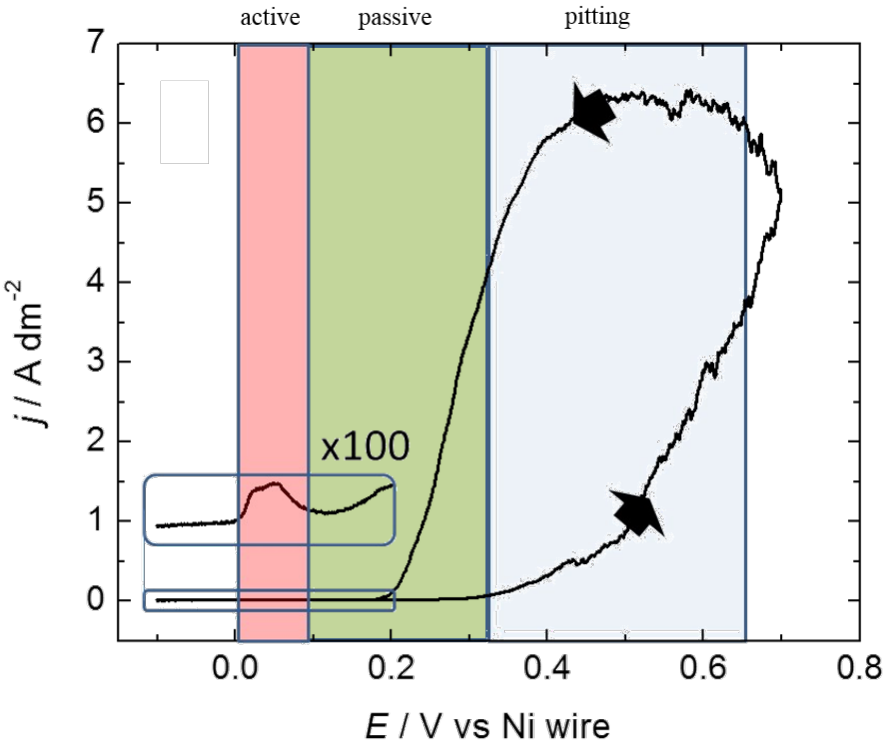

Figure 4-1: Linear sweep voltammagram of the anodic polarization regions for Ni in Watts' electrolyte. The active region is shown in red, the passive region in green and the pitting region in blue. Arrows note the direction of the scan and the inset shows the active peak magnified 100x.

4.2 Potentiostatic Dissolution

4.2.1 Active Region

To examine the surface evolution of polished Ni electrodes in various regions of the polarization curve, potentiostatic dissolution was monitored using *in situ* time-lapse optical imagery. The electrode surface had an air-formed oxide and was exposed to the solution only briefly at open circuit potential prior to application of the desired potential. For $E = 0.050$ V time-lapse captures corresponding to 0 and 100 minutes are shown in Figure 4-2 a) and b) respectively and illustrate that the surface evolution is a slow process. Pitting does not occur in this region, which is consistent with $E_p = 0.320$ V. After 100 minutes the surface has a pebbled appearance that is the result of preferential dissolution at grain boundaries, which has been reported elsewhere for active dissolution.[6] The ridges that appear in the surface are the result of the layer-by-layer method by which the pellet was made. The layer-by-layer structure consists of domains of micro-scale and nano-scale grains in a pattern of rings. Dissolution current is expected to vary widely between domains of different grain sizes due to the large difference in grain boundary density. The current density for the experiment was initially small, around 0.007 A dm^{-2} and decreased over the first 100 minutes. Beyond 100 minutes the current density was around 0.002 A dm^{-2} corresponding to the level measured for passive potentials.

4.2.2 Passive Region

In situ time-lapse images for $E = 0.300$ V show no surface evolution of the surface over the 180 minute experiment. Comparing Figure 4-2 c) and d), a single pit can be noted in Figure 4-2 d) that became visible within the first minute of the experiment. The appearance of the pit is identical after 180 minutes of passive polarization indicating that it repassivated early in the experiment and is by definition, metastable. Metastable pitting at $E = 0.300$ V is consistent with $E_p = 0.320$ V. No additional metastable pits were observed after the first minute, which suggests that passivity breakdown was highly correlated with the potential step at the start of the experiment. However, additional metastable pits may have formed outside of the field of view or may have been invisible by optical microscopy. In general, processes giving rise to the passive current density caused no observable change to the electrode surface over 180 minutes. The

current density decreased to passive levels within 5 s of the application of the potential and remained at this level for the duration of the experiment.

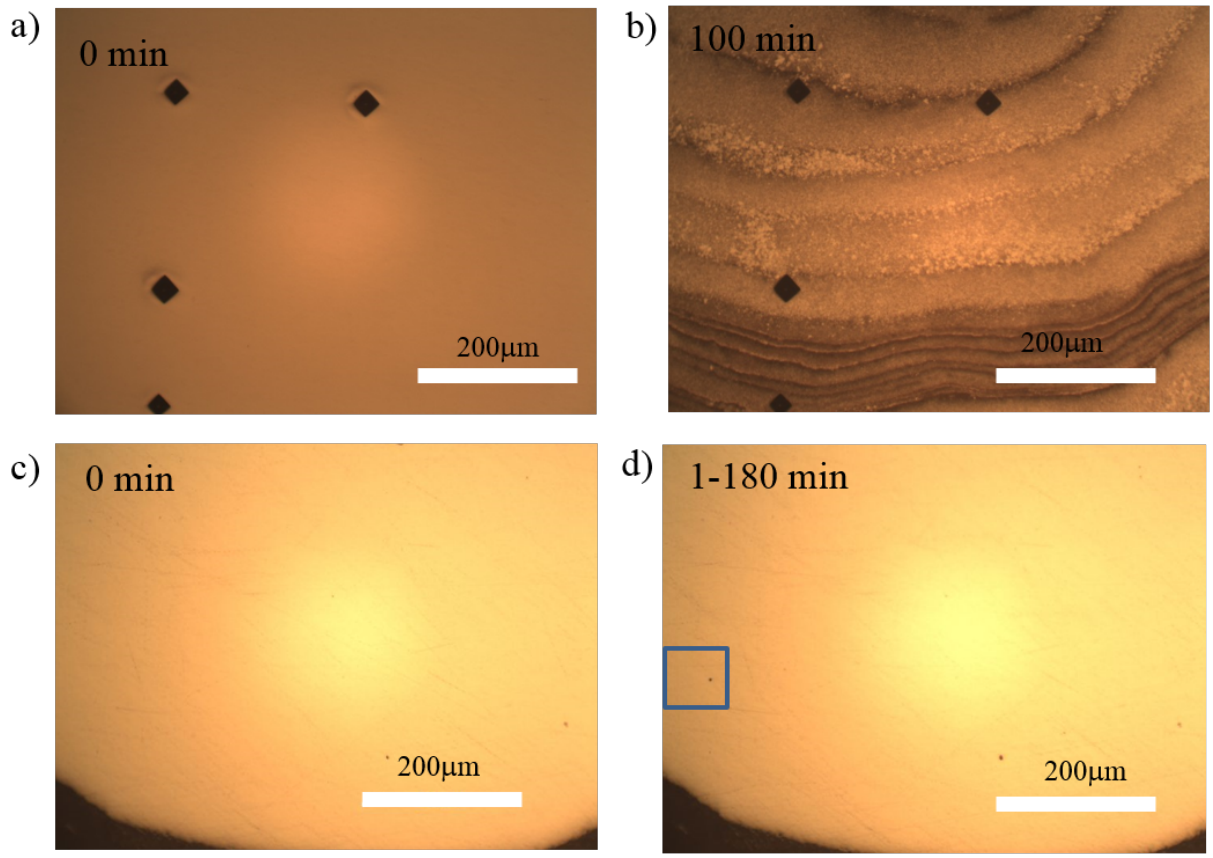

Figure 4-2: *In situ* optical captures for potentiostatic treatment at 0.05 V in a) and b), and 0.3 V in c) and d). A single metastable pit is indicated in panel d). Diamond shapes in a) and b) are Vickers hardness indents used as fiduciary markers.

4.2.3 Pitting Region

Ni electrodes treated potentiostatically above E_p showed pitting in clusters of pits that propagated beneath metallic covers. Even at the largest potential examined, E = 1.0 V, large open pits were not observed. Upon removal of the electrode from the cell, pit covers remained intact indicating that they were quite robust, although they could be mechanically removed with tape for examination of the underlying pit interior. Figure 4-3 contains *in situ* optical images of the pitted surface for an applied potential of E = 0.8 V in panels a) through d). Careful analysis of panels a) through c) indicated that all propagating pits within the field of view nucleated

within the first minute of the experiment. Large regions of the surface did not contain any pit nuclei. Pit nucleation is clearly dependent on the structure of the substrate metal because clusters of pits were correlated to the ring structure of the Ni pellet. Lacy pit covers were observed at higher magnification after completion of the dissolution and a representative image is shown in Figure 4-3 d). For all potentials investigated in the pitting region, pit interiors were electropolished indicating they were probably covered by a bilayer salt film consisting of a thin film of $NiCl_2$ under a thick porous film of $NiSO_4$.[2,4,5,7,8] A low magnification optical image of electropolished pits after mechanical removal of the pit covers is shown in Figure 4-3 e). Although the initial pit nucleation was highly correlated with certain rings in the structure of the pellet, it is not apparent after completion of the dissolution. Propagation of electropolished pits does not appear to be confined by the underlying layer structure of the Ni pellet because pits remained roughly hemispherical even as they became quite large. A high magnification SEM image in Figure 4-3 f) shows the surface morphology of an electropolished pit interior.

For potentiostatic dissolution at E = 0.6 V, 0.8 V and 1.0 V the average current densities were 4.0, 9.5 and 9.9 A dm^{-2} respectively. The current density rose quickly to a plateau and then fluctuated around this value. Because sustained potentials above E_p lead to high current densities, which are linked to lower residue, two important aspects of these pits should be noted, pit covers and electropolishing. Since lacy pit covers were present at high potentials and high current densities, their contribution to residue should either decrease with increasing current density or represent a minimum baseline residue level. In the case of the latter, the pit interior should be the main cause of increased residue at low current densities. Any differences between the electropolished pit interiors (high potential and high current density) and those that grow during galvanostatic dissolution at low current density (< 1 A dm^{-2}) should be considered suspect for increased residue.

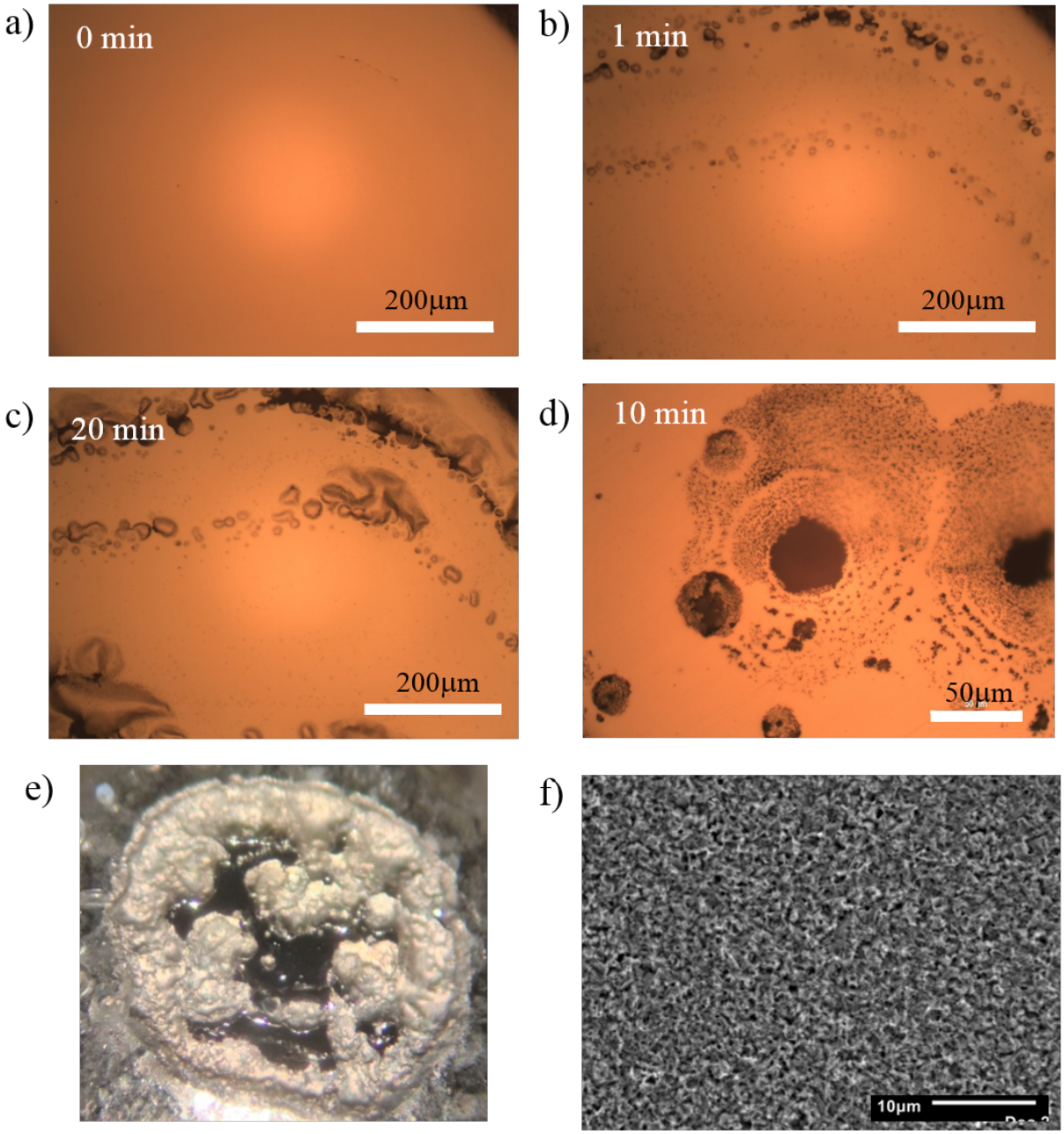

Figure 4-3: *In situ* captures showing potentiostatic pitting at 0.8 V in panels a) through c). High magnification *ex situ* optical image after dissolution d). Low magnification optical image of the entire electrode surface after mechanical removal of the pit cover e). High magnification SEM of an electropolished pit interior f).

4.3 Galvanostatic Dissolution

Galvanostatic experiments using a current density of 0.4 A dm^{-2} were performed with *in situ* observation of the electrode surface to examine pitting behavior at a low current density known to produce high residue levels. Figure 4-4 a) shows the potential-time trace collected for a representative experiment. Immediately after the current was applied, the potential spiked greater than 1.0 V, which caused passivity breakdown and pit nucleation. The potential then decreased over several minutes and fluctuated around $E = 0.45$ V for nearly 20 minutes. A second period of potential spikes occurred around 23 minutes and persisted for about 15 seconds followed by another region where the potential decayed slowly to near passive levels. Based on the pitting corrosion literature, the behavior associated with this potential transient could be described as follows. At the moment the current is applied, a large number of pits must nucleate to supply the desired current density because the current from each pit is small. Since the pit current should increase with t^2 at short times, a large fraction of the nucleated pits must repassivate to maintain a constant current density, and the potential decreases rapidly throughout this stage to promote pit repassivation. Pits that survive must reach temporary stability and should transition to a $t^{1/2}$ growth regime. This rate change presumably causes the potential to stabilize around $E = 0.45$ V. Small fluctuations in the potential during this stage are interpreted as a result of changes in the metallic pit covers.[1,3] Such fluctuations have also been attributed to electropolishing salt films, however as will be shown later, the appearance of the pit interiors is inconsistent with an electropolished surface. Eventually pit growth is insufficient to maintain the desired current and the potential spikes again, nucleating new pits.

The evolution of the surface during the first 30 minutes of the transient is illustrated in Figure 4-4, which contains *in situ* optical images of the electrode surface corresponding to 0, 1, 20, and 30 minutes of dissolution in panels b) through e) respectively. By comparing panels b) and c) any pits that were nucleated immediately following the initial potential spike are identified. Beyond the first minute of the experiment, all but two of the pits showed no visible growth and probably repassivated. Pits that noticeably propagated beyond the first minute did so beneath a lace-like pit cover that was composed of undercut metal. They are indicated in panel c), however the lace-like pit cover is not obvious until 20 minutes dissolution in panel d).

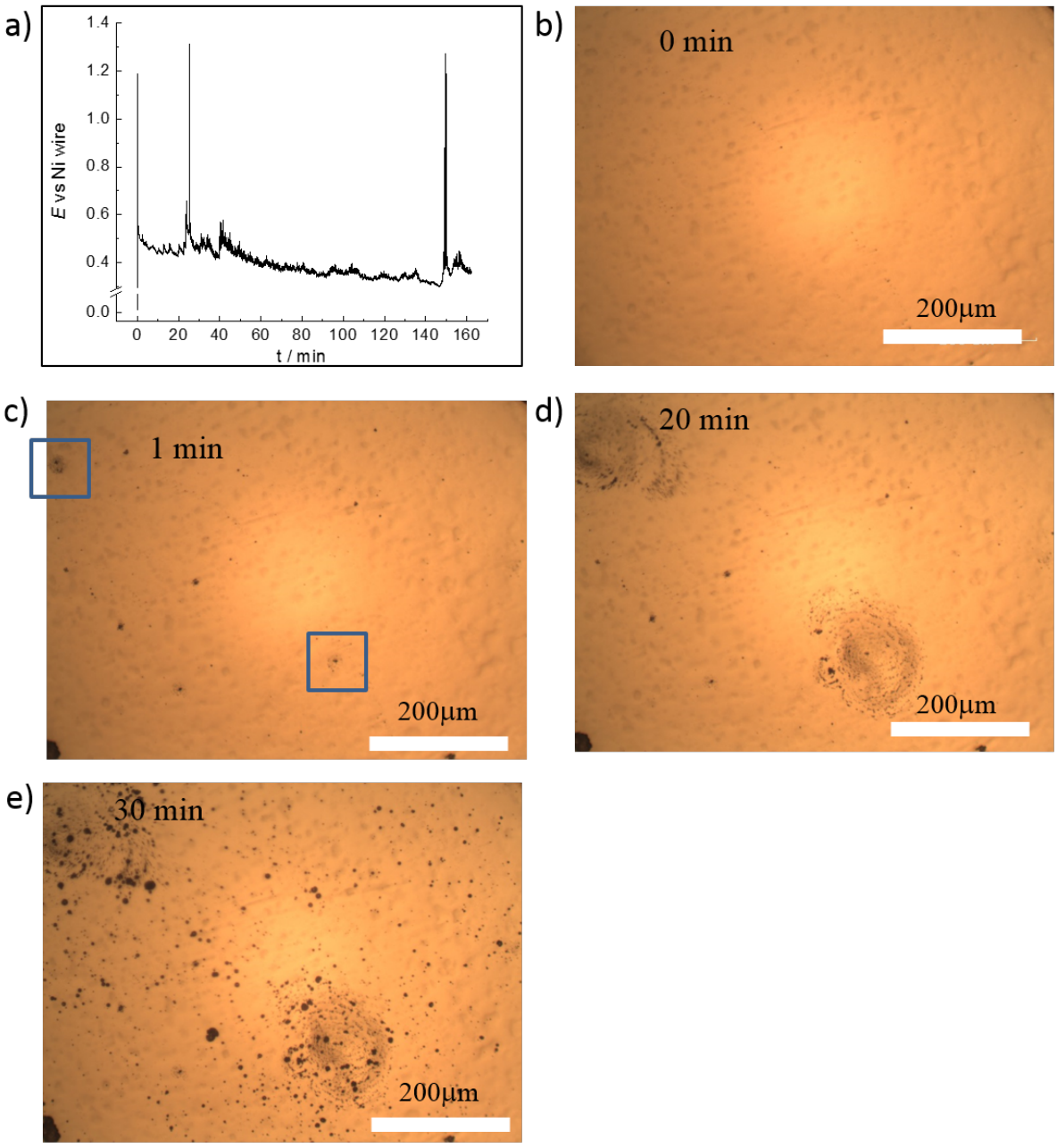

Figure 4-4: Potential time plot for a galvanostatic experiment at 0.4 Adm^{-2} in a). Corresponding *in situ* optical captures b) through d).

Perforations in the pit covers in d) appear in a pattern of concentric rings that has been described previously for covered pits in stainless steel.[1] Additional pit nucleation was correlated with potential spikes that occurred around 25 minutes, which is illustrated in panels d) and e). While a large number of new pits appeared on the surface, they did not appear to propagate. Presumably

these potential spikes resulted in a small population of pits that continued to grow under a metallic cover, however none were found inside the microscope field of view. Furthermore, no additional growth of the two initial lacy-covered pits was observed after 25 minutes indicating that they probably repassivated.

If it is assumed that no new pit nucleation took place in the time interval 1-20 minutes, then any pits that had not repassivated attained temporary stability. They are described as temporarily stable because at a constant potential they should be stable and have a current that increases with $t^{1/2}$. However, in the galvanostatic experiment they are temporarily stable because their growth must be slowed to maintain a constant current. This is evidenced by the slowly decaying potential during this time interval. The implications of this behaviour should be discussed in terms of the pit stability product. Recall from Chapter 2, section 2.4.4 that a pit current increasing with $t^{1/2}$ corresponds to a constant pit stability product. On the other hand, for a constant pit current, the pit stability product must decrease in time. Since the pit stability product is proportional to the enrichment of corrosion products at the pit surface, the concentration of corrosion products at the pit surface must also be decreasing. Even if pits propagate initially as electropolished hemispheres, the decreasing concentration of corrosion products at the pit surface will eventually lead to a situation where pits begin to propagate as crystallographic etch pits. This transition from electropolished hemispherical pitting to crystallographic etch pitting has been described previously for stainless steels under conditions of decreasing potential.[9-11] Then for Ni in Watts' electrolyte one can make the conjecture that low current density galvanostatic dissolution leads to the prolonged propagation of crystallographic etch pits, which should be suspected as a major contributor to anode residue.

4.4 Pulsed Potential Dissolution

4.4.1 Current Transients

Current transients were collected after stepping the potential from 0 V to potentials of 0.6 V, 0.8 V, 1.0 V and 1.2 V and representative traces are shown in Figure 4-5 a) through d) respectively. In general the current at all times was higher with increasing potential. This is mostly due to an increased density of pits on the surface but also may be convoluted with higher pit current density, which has been described previously.[3,12] All transients show the same general

features and the shape for each was remarkably repeatable when electrodes were repolished and the oxide layer was allowed to reform. All transients exhibit an initial current spike and decay at short times that can mostly be attributed to charging of the electrical double-layer. This is not as obvious in Figure 4-5 a) because the transient was collected at a much lower sampling rate due to its long duration. Current in this section of the transient is not wholly attributed to double-layer charging because as will be shown later, Ni dissolution takes place within the first 50 ms. A similar transient was collected in a Cl^- free electrolyte for a step from 0 V to 1.2 V that gave the double-layer charging in the first few seconds and is shown in Figure 4-5 d) in green. In general transients could be fit to Equation 4.1 where j and $(t - \tau)$ are the electrode current density and corrected time respectively and a and b are constants. Fits are represented by the red traces in Figure 4-5. For each transient the data was fit to Equation 4.1 with $x = 2$ at early times, while it was fit with $x = 0.5$ at longer times. At intermediate times a transition region between the two regimes of growth is observed which was not fit to Equation 4.1. Because the current is from an ensemble of pits in the same general growth regime, the nucleation events should be highly correlated in time and passive-layer breakdown is highly correlated with the potential step.

$$j = a(t - \tau)^x + b \qquad [4.1]$$

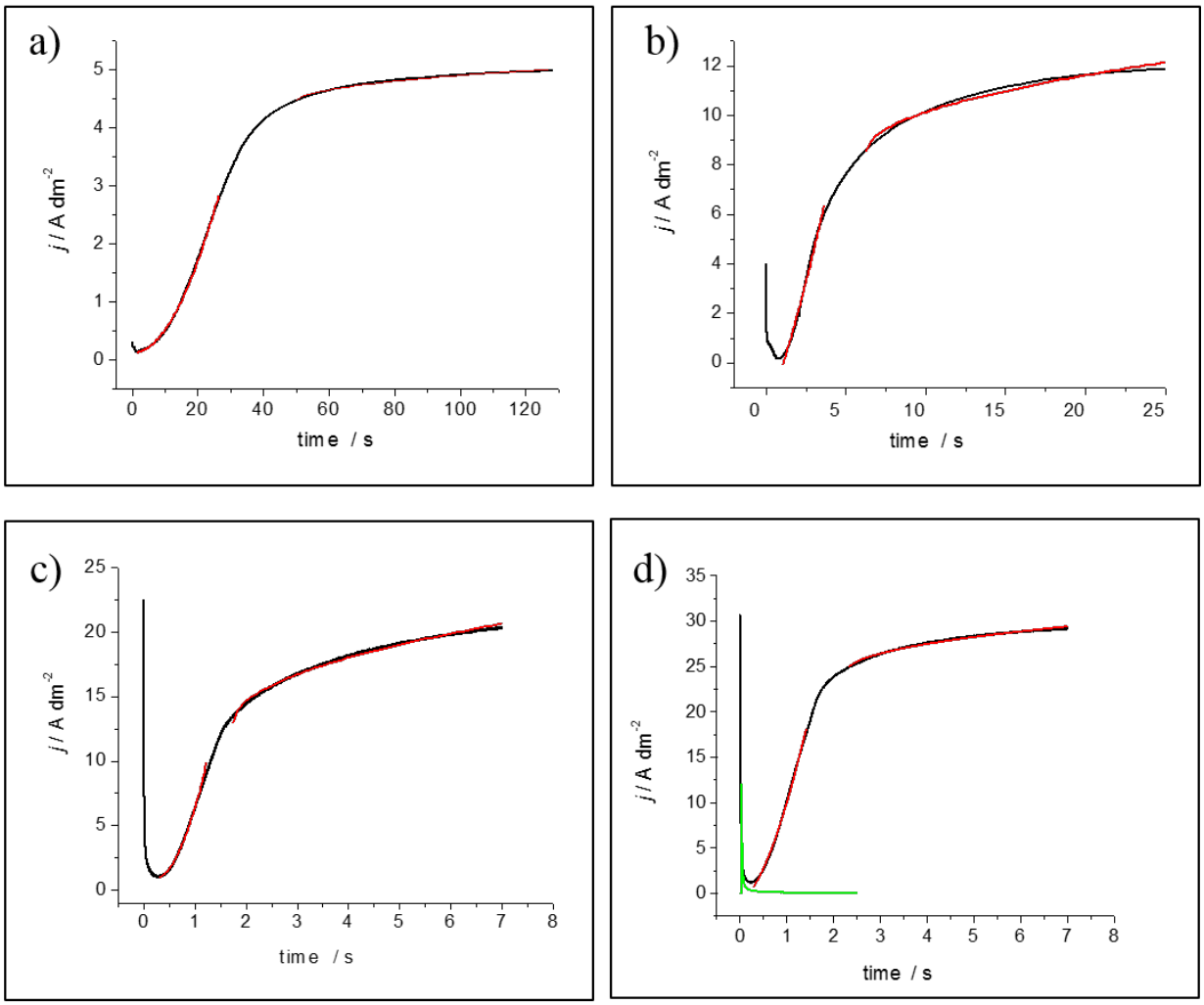

Figure 4-5: Current transients for a potential step to 0.6 V, 0.8 V, 1.0 V, and 1.2 V in a) through d) respectively. Fits to Equation 1 are shown in red. Double-layer charging in chloride-free electrolyte is shown in green in panel d).

The transition from t^2 to $t^{1/2}$ is discussed in the literature and since $t^{1/2}$ is only predicted for an open hemisphere, the transition has been attributed to the loss of the pit cover.[3,12] However, if one considers the two possible limiting currents, a change in rate without any loss of the pit cover can also be envisioned. Recall that for a current that increases with t^2, the pit current density is constant with changing radius. While for a current that increases with $t^{1/2}$, the pit current density decreases according to $1/r$. These two pit current density functions are plotted for a hypothetical pit in Figure 4-6. Since flux and pit current density are directly proportional, the green trace can be thought of as the flux permitted through the pit mouth, while the black

trace can be thought of as the flux from the pit surface. The actual measured current will be the smaller of the two limiting cases. If the hemispherical flux from the pit surface is larger than the flux permitted through the pit mouth then the smaller constant flux should be observed. Once a transition radius, r_T is reached, the flux from the pit interior becomes smaller and a rate change will be observed in the current transient. In other words, the rate-determining flux switches from transport across the pit mouth to transport from the pit surface. In this view the observation of a rate change does not give any information regarding the presence or absence of a pit cover. It does however, signal a transition to a regime where the growth rate becomes entirely independent of the status of the pit cover.

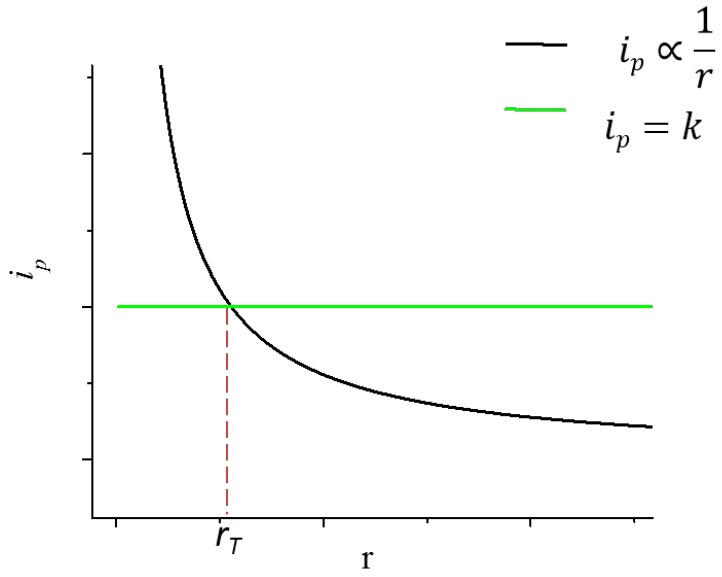

Figure 4-6: Plot of the two possible pit current densities as a function of pit radius for a hypothetical pit. The green trace is the rate limiting flux is across the pit mouth. The black trace is the flux from the hemispherical pit surface. The transition radius, r_T, is the radius at which a rate change should be observed.

The time at which the rate change is observed is dependent on the relative flux permitted through the pit mouth and the flux from the growing pit interior. For 0.6 V, the transient followed t^2 dependence for 26 s, while for 1.0 V and 1.2 V this growth regime only persisted for less than 2 s. If the pit current during this growth regime is diffusion limited by a pit cover, then one must explain this potential dependence. According to Pistorius and Burstein the effect of

increased potential is to make more open sites on the surface susceptible to pitting.[3] In this case, more open sites must have a pit cover that permits higher flux and/or ruptures sooner to explain the trend. If pit growth is limited by the ohmic resistance of the cover, then the trend is easily explained. The current from the pit should increase with increasing potential and the rate change is observed sooner because pit growth is more rapid as the applied potential is increased.[12] The trend can also be explained in the context of PDM. PDM predicts that the applied potential has two roles in pit generation, to generate cation vacancies at the film-electrolyte interface and to drive their transport to the metal-film interface. Increasing the potential makes more sites on the surface susceptible to pitting by increasing the vacancy flux. Since flux is exponentially dependent on the applied potential, voids should also grow at an increased rate.[13-15]

4.4.2 Effect of Pulse Potential

To examine the effect of potential on pit density and morphology for short growth times, potential pulses were applied to polished electrodes and the pits imaged *ex situ* with optical microscopy. Figure 4-7 shows the resulting electrode surfaces after 200 pulses of 2 s for potentials of 0.6 V, 0.8 V, 1.0 V and 1.2 V in panels a) through d) respectively. A potential of 0 V was applied for 3 s in between pulses so that the pits could repassivate, which was confirmed by a return to near-zero current density. As expected there was an obvious increase of pit density on the surface as the potential was increased. When the pulse potential was 0.6 V, most of the electrode surface remained pristine with the exception of some dissolution along specific rings of the anode ring structure. The dissolution current during the initial 2 s of the $E = 0.6$ V transient (Figure 4-5 a)) is small and corresponds to the beginning of detectible pit current. A potential of 0.8 V gave a small number of open hemispheres with electropolished centers, however many appear dull and non-hemispherical. For $E = 0.8$ V a time of 2 s corresponds to the transition region of the transient (Figure 4-5 b)) where the current is approaching $t^{1/2}$ behaviour and a mixture of morphologies is expected. When the potential was increased to 1.0 V, most pits were hemispherical and had an electropolished appearance. The current transient at this potential (Figure 4-5 c)) has clearly transitioned to $t^{1/2}$ behaviour at 2 s and the transition for $E > 1.0$ V should be associated with the onset of electropolished appearance caused by precipitation of a thick, porous salt film. For $E > 1.0$ V, most pits were not covered indicating that covers were either lost *in situ*, optically invisible, or had been removed mechanically during sample transfer.

For E = 1.2 V pits have the same general hemispherical, electropolished appearance and pit density on the surface increased to the point where the growth of many hemispherical pits overlapped. The trend followed similarly for E > 1.2 V. However, as the potential approached 2 V, there was a marked change in the shape of the transient that was attributed to significant current from competing reactions. The remainder of the pulse experiments were done with E = 1.2 V due to large density of pit nuclei that could be obtained on the surface.

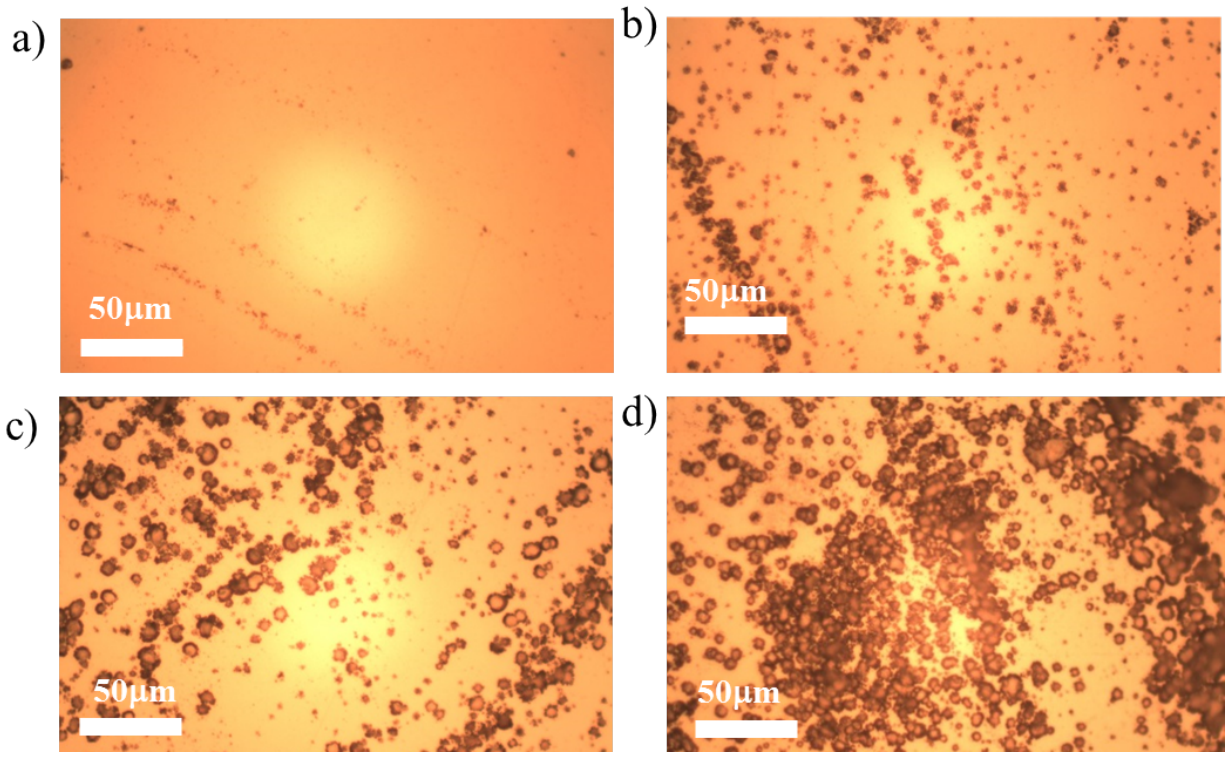

Figure 4-7: Ex situ optical images showing the change in pit density and morphology for a series of potential steps to 0.6 V, 0.8 V, 1.0 V and 1.2 V in panels a) through d) respectively.

4.4.3 Analysis of Individual Pits

For a E = 1.2 V pulse, pits were examined *ex situ* using SEM after 100 pulses for pulse times of 50 ms, 200 ms, 300 ms, 500 ms and 700 ms and representative images are found in Figure 4-8 a) through e) respectively. As in the previous section, E = 0 V was applied to the sample in between pulses for sufficient time that the current density returned to near-zero values signaling pit repassivation. After 100 pulses, the density of pits on the surface was sufficiently

low that individual pits were spatially separated and could be individually analyzed. For a pulse time of 50 ms, the surface showed no observable change by SEM. For a pulse time of 200 ms, a low density of small pits became visible by SEM. For pulse times greater than 300 ms, hemispherical pits were observed that appeared as dark circular spots, surrounded by a bright halo. Because the images were collected using the secondary electron signal, contrast is due to a combination of topographical features and edge effects. The pit interior appears dark because electrons leaving the sample from the pit interior have an obstructed path to the detector. The reverse is true for features that have a less obstructed path and they appear brighter. However, this is convoluted with edge effects that contribute additional brightness. Edge effects are observed when the teardrop shaped interaction volume of the beam coincides with a large area of outer surface from which electrons can escape the sample and reach the detector. If the halos are the result of edge effects, one interpretation is that there is a thin, metallic partial pit cover that protrudes over the pit from the pit edge.

Because SEM is limited to a qualitative topographical assessment of the surface, WLIM was used as a complimentary technique to obtain quantitative surface profiles. WLIM gives nanometer depth resolution while at the same time providing sub-micrometer spatial resolution. Representative WLIM images for samples pulsed 100 times at $E = 1.2$ V for pulse times of 200 ms and 700 ms are shown in Figure 4-9 a) and b) respectively. Figure 4-9 c) shows a plot of pit depth versus pit radius that was generated using extracted line profiles for individual pits from multiple WLIM images. The impression of a more densely pitted surface for a pulse time of 200 ms is an artifact of the scale in which the images are presented. For the 700 ms pulses, a small number of pits have grown to a depth that requires a much larger vertical scale, and a large number of pits that did not grow beyond a superficial stage are invisible due to lack of contrast.

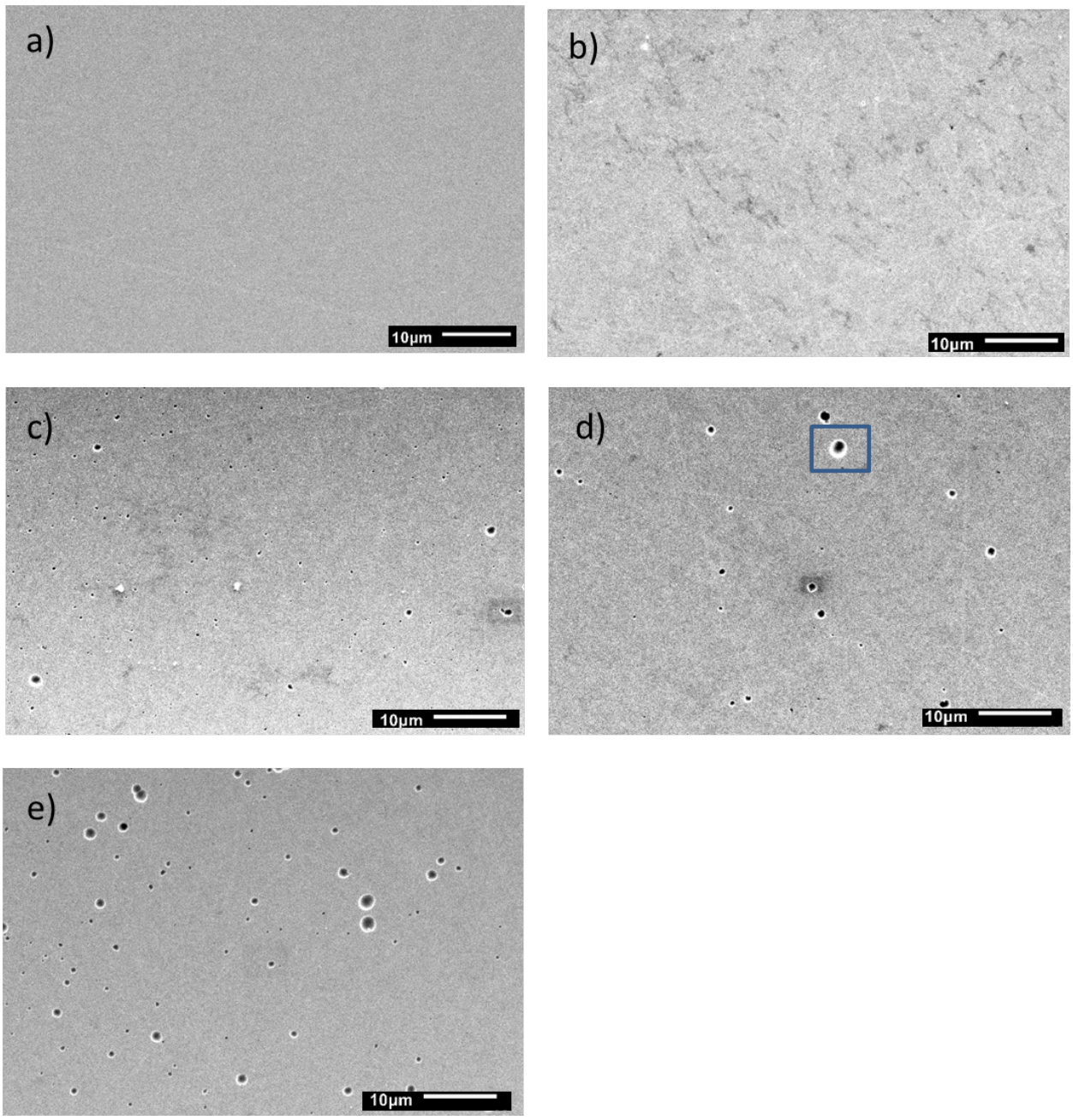

Figure 4-8: SEM images of samples pulsed 100 times at 1.2 V. Pulse times are 50 ms, 200 ms, 300 ms, 500 ms, and 700 ms in panels a) through e) respectively. A bright halo from a protruding partial metallic cover is indicated in d).

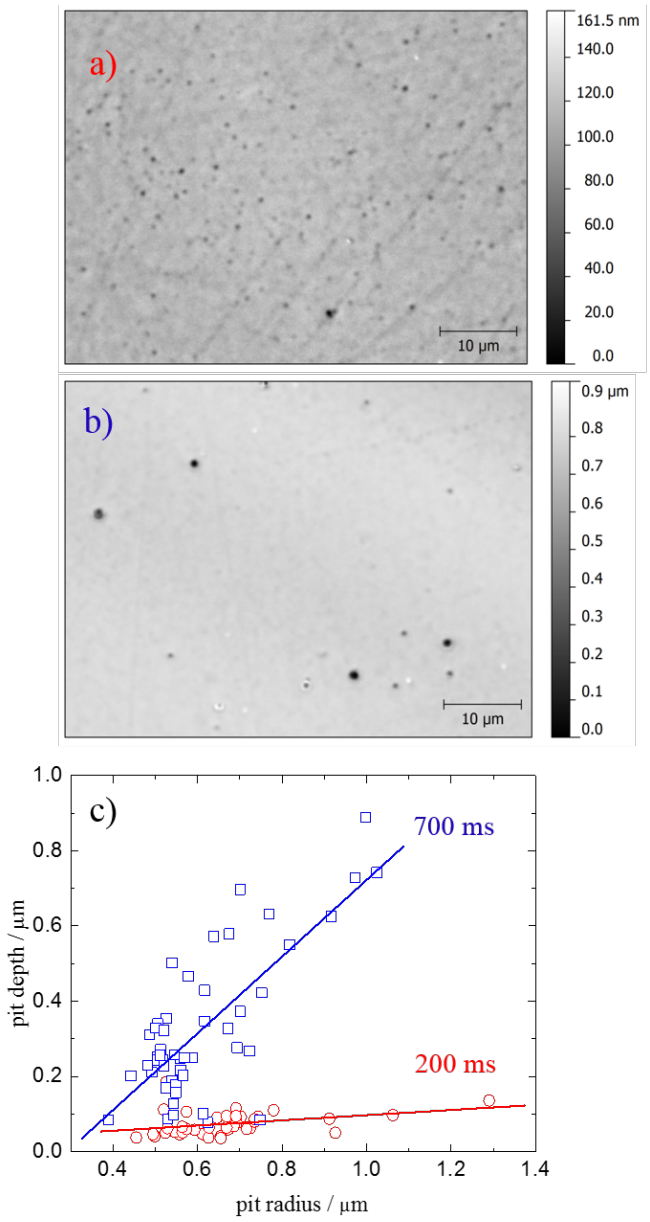

Figure 4-9: WLIM images for 100 pulses at 1.2 V for times of 200 ms and 700 ms in a) and b) respectively. Plot of pit depth versus pit radius for pulse times of 200 ms (red) and 700 ms (blue) in c). Slopes of trend lines are 0.07 for 200 ms and 1 for 700 ms.

For a pulse time of 200 ms, the plot of pit depth versus pit radius in Figure 4-9 c) gave a trend line slope of 0.07, indicating that the features are superficial with a depth much smaller than the radius of the feature in the plane of the electrode. According to the transient in Figure 4-5 d), this pulse time corresponds to a region of the transient prior the onset of detectible t^2 growth. One explanation for the depressions in the surface is voiding at the metal-film interface.

Since the passive film should be optically invisible, the result from WLIM is a measurement of the void in the metal surface. Such voids have been proposed for penetration models and film breaking models of passivity breakdown and pit nucleation.[13-15] The same result could occur if passivity breakdown were to take place via adsorptive thinning. However, thinning prior to uncovered pitting should be limited to several nanometers (ie the thickness of the passive film), which is much shallower than the depth of superficial pits as measured by WLIM. For the case of a more robust pit cover that is optically reflective, the depressions could correspond to a pit cover that is intact but sunken due to a void in the bulk metal underneath. In this case the pit cover should be composed not only of surface oxide, but also bulk metal so that it is optically reflective.

For a pulse of 700 ms duration, the plot of pit depth versus pit radius had a trend line with a slope of 1, indicating that the pits as measured by WLIM are nearly hemispherical. The current transient for E = 1.2 V in Figure 4-5 d) shows that 700 ms is within the region of t^2 growth, where pitting should be under a growth-limiting pit cover. Because these samples were imaged *ex situ*, any fragile pit covers that may have been present could have been damaged or removed during sample transfer and rinsing. Furthermore if pit covers were intact and consisted merely of remnants of the original passive layer they should be optically invisible. The hemispherical pits imaged by WLIM represent only a small fraction of the total pit nuclei, while the remainder may have repassivated in an earlier stage of growth where they remain superficial.

4.4.4 Analysis of 10^4 pulses

To understand the surface evolution of electrodes during long time-scale pulsed electrodissolution experiments, samples were pulsed 10^4 times using the same pulse sequences as described in the previous section. The extent of dissolution should be roughly 100 times greater than for the previous pulse experiments and more pronounced changes should be seen. Figure 4-10 shows SEM images of the electrode surfaces collected after 10^4 cycles for pulse times of 50 ms, 200 ms, 300 ms, 500 ms and 700 ms in panels a) through e) respectively. For a pulse time of 50 ms, metal dissolution is evident and concentrated at the grain boundaries of Ni. Since pit growth is limited for such a short pulse, mechanisms leading to pit nuclei must be concentrated at metal grain boundaries. This can be satisfactorily addressed using film breaking and PDM models of passivity breakdown, because each considers that localized breakdown takes place at

weak points or defect sites in the oxide structure, which should be dependent on the underlying metal.[13-15]

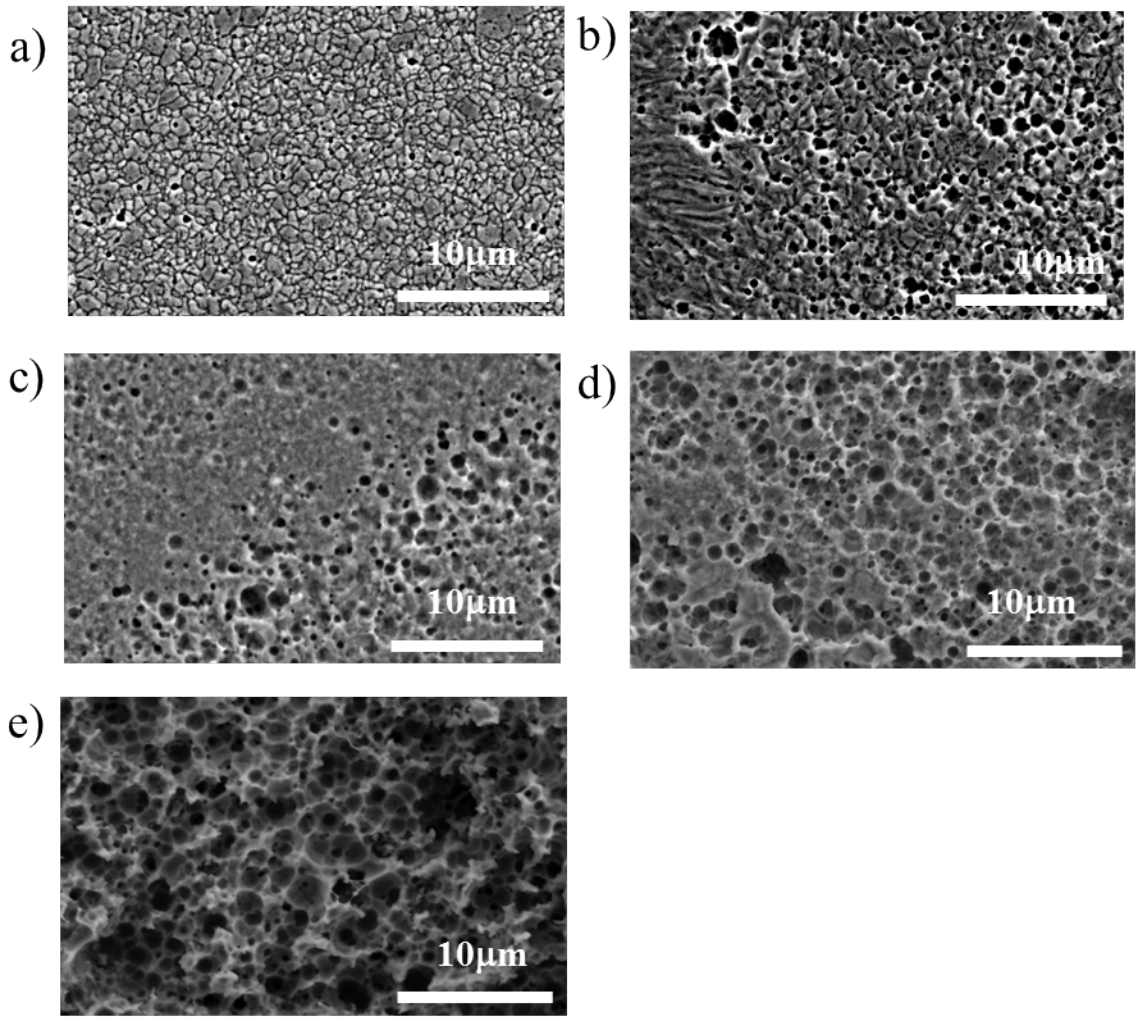

Figure 4-10: SEM images for samples pulsed 10^4 times at 1.2 V with a repassivation phase at 0 V between pulses. Pulse times are 50 ms, 200 ms, 300 ms, 500 ms, and 700 ms in panels a) through e) respectively.

As pulse times increased into the t^2 region of the current transient, there is a general trend toward porous, rougher surfaces because a larger portion of the total metal dissolution comes from hemispherical pitting. For pulse times of 200 ms the resulting surface has noticeable contributions from superficial grain boundary dissolution as well as hemispherical pitting. For

pulse times ranging from 500 ms to 700 ms, hemispherical pits completely cover the surface with no observable superficial grain boundary dissolution because the amount of dissolution in the first 200 ms is small compared to the contribution from hemispherical pitting.

Most importantly, these experiments show that using short potential pulses of $E = 1.2$ V is an effective route to alter anode pitting, which in turn alters the surface evolution over long times. Since high amounts of residue is produced when large, covered pits grow at low potentials, small, open pits grown for a short time at large potential are attractive for residue mitigation.

4.4.5 Analysis after 85 hours

A pulse time of 50 ms and $E = 1.2$ V was used to compare the anode surface for the pulsed method to that of galvanostatic dissolution over long times. The pulse time of 50 ms was chosen due to the relatively flat surface morphology after 10^4 pulses. In addition the surface of the 50 ms pulsed sample contained the least amount of total metal dissolution after 10^4 pulses, and the result of an extended experiment would be expected to show the largest difference in surface morphology. The 50 ms, $E = 1.2$ V pulse was followed by 60 ms at $E = 0$ V (45% duty cycle) so that the average current density (0.33 A dm^{-2}) closely matched the current density of the galvanostatic experiment (0.36 A dm^{-2}) for comparison. To measure the current density for the pulsed method, the current was integrated after each complete cycle and cumulatively added to give the total charge, which was divided by the total time and initial electrode area to give an average current density. By integrating the complete pulse sequence any contributions to the anodic current from double-layer charging were negated by discharging during the $E = 0$ V phase and any dissolution current during the $E = 0$ V phase also contributed to the measured current. Both methods were run around 85 hours and were estimated to have lost less than 5% of the original anode mass. Low-magnification SEM images for the galvanostatic and pulsed experiments illustrate a marked difference between the electrode surfaces. The low-magnification image of the galvanostatic sample in Figure 4-11 a) shows typical covered pitting, with a large torn pit cover visible in the center of the image surrounded mostly by a pristine polished electrode surface that has been undercut. Additional pit openings are visible around the torn covers however they are present on only a small fraction of the surface. In general the surface consisted mostly of pristine polished surface. The low-magnification SEM image for the

pulsed dissolution experiment in Figure 4-11 b) shows a homogeneous texture and the image is representative of the entire surface. This indicates dissolution from the same mechanism everywhere, although the rate was not equal across the surface as evidenced by depressed areas in the image.

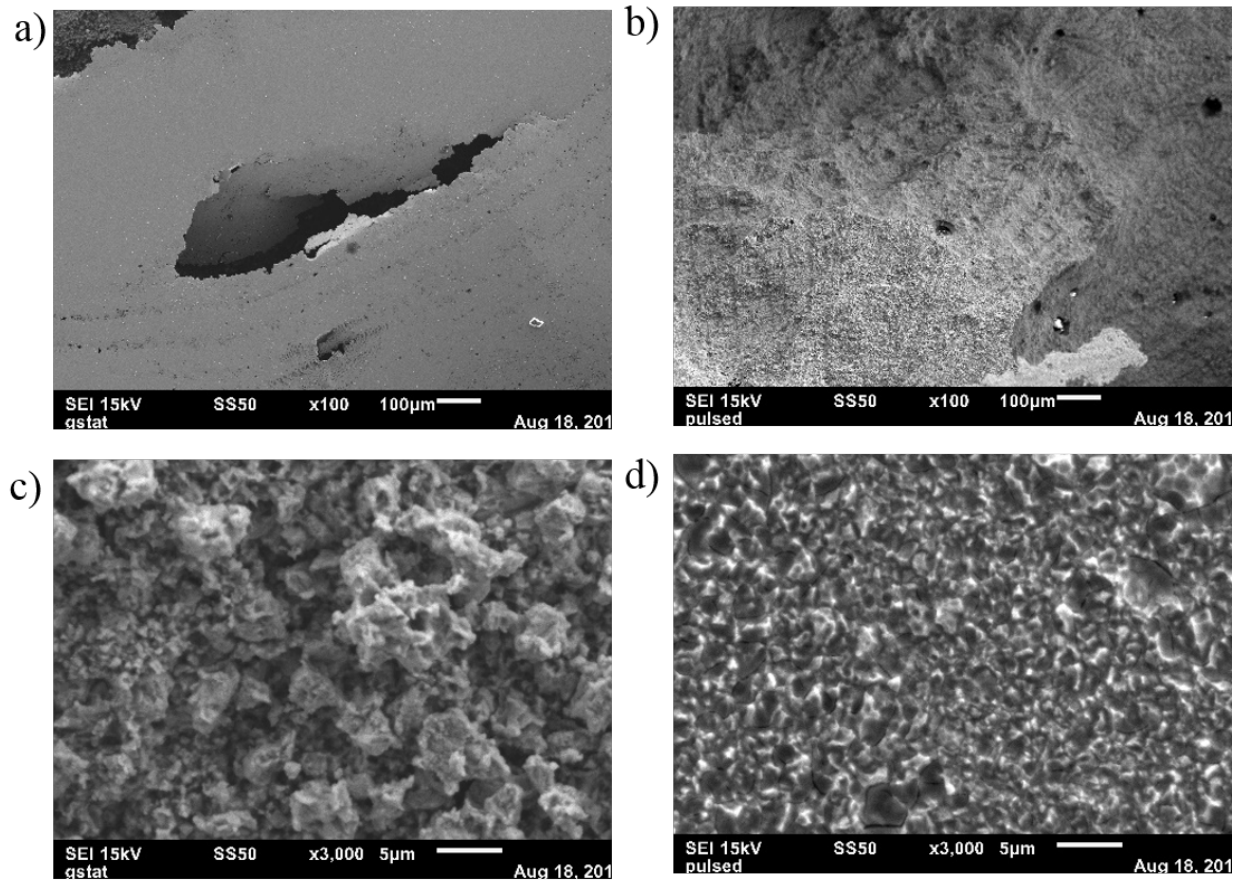

Figure 4-11: Low magnification SEM image after 85 hours of galvanostatic dissolution in a), and pulse dissolution in b). Panel c) show a high magnification SEM image of the pit interior of the galvanostatic sample and d) shows a high magnification image of the pulsed dissolution surface.

Figure 4-11 c) shows a high-magnification SEM image of a pit interior for the galvanostatic sample. It has a qualitatively roughened surface and notable particulate appearance. This surface is taken to be crystallographic etch pitting where the corrosion rate is slow and crystallographic nature of the metal dictates corrosion rates. In contrast, the high-

magnification image of the pulsed surface in Figure 4-11 d) is comparatively smooth with a texture closer to that of an electropolished pit. The similarity between the pulsed surface and an electropolished pit suggests that the pulsed surface should produce similarly low residue. Intuitively, one would predict the rougher, particulate surface of the crystallographic etch pit interior leads to more particles that detach from the bulk and end in residue. This set of images illustrates two extremes of pit nucleation and growth. The galvanostatic method results in a small number of pits that grow for an extended period of time at low potentials and low pit current density. On the other hand, the pulsed method results in a high number of pit nuclei and an intentionally short growth time that produces small pits with high pit current density.

4.4.6 Residue Quantification

To quantify and compare residue levels from pulsed dissolution to those of galvanostatic dissolution, repeat trials of the previous 85 hour experiments were done and the anode residue collected. The cathode efficiencies for the pulsed and galvanostatic methods were identical within experimental error (98 +/- 1%) so the residue amounts could be normalized to the cumulative charge for relative comparison. A total of 16 pellets were used for each dissolution method in 4 repeat experiments, each using an anode assembly consisting of 4 pellets to give a large enough sample size that pellet-to-pellet variations would be reduced.

The relative amounts of Ni as residue for the two methods, as determined by flame atomic absorption are shown in Figure 4-12. The amount of Ni residue was reduced more than six-fold for the pulsed method as compared to galvanostatic dissolution. A mass based quantification of residue was attempted however on the small scale of these experiments, the error associated with the mass difference measurement was nearly as large as the mass of residue and the method was abandoned. Ideally any quantitative residue experiments should be performed for a much longer time scale because the relative residue after < 5% mass dissolution may not reflect the amounts after complete dissolution. Due to the low current density of the experiments and the need to sample an adequate number of individual pellets for each method, time constraints limited each trial to 85 hours. If the Ni content of the residue is taken as representative of actual residue, this result confirms that two suspected sources of anode residue can be reduced on a laboratory scale by carefully controlling pit growth.

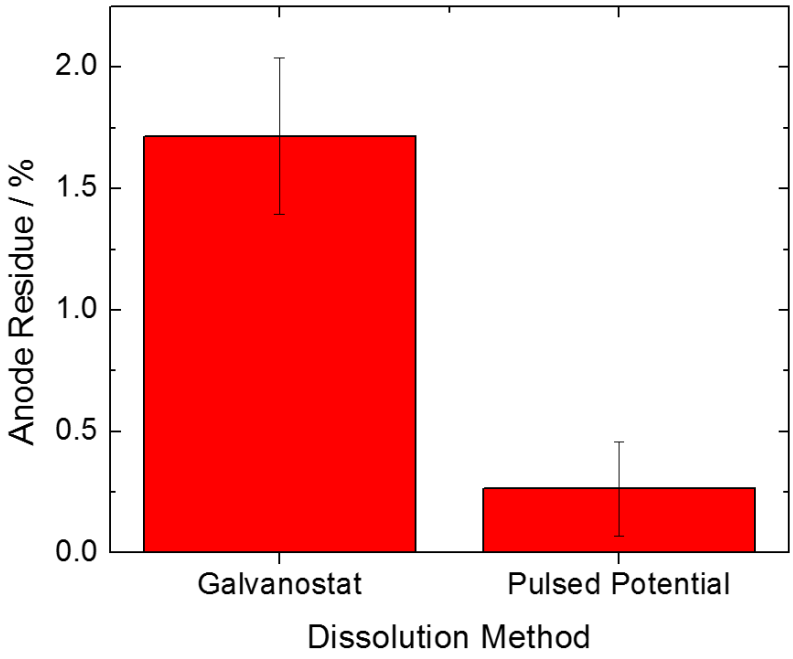

Figure 4-12: Comparison of the relative amounts of anode residue for galvanostatic and pulse potential electrodissolution. Error bars represent the standard deviation of the repeat trials for each method.

4.5 References

[1] Laycock, N.J.; White, S.P.; Noh, J.S.; Wilson, P.T.; Newman, R.C. *J. Electrochem. Soc.* **1998**, *145*, 1101-1106.

[2] Strehblow, H-H.; Wenners, J. *Electrochimica Acta*, **1977**, *22*, 421-427.

[3] Pistorius, P.C.; Burstein, G.T. *Phil. Trans. R. Soc. Lond. A*, **1992**, *341*, 531-559.

[4] Laycock, N.J.; Newman, R.C. *Mater. Sci. Forum.* **1995**, *649*, 194-194.

[5] Laycock, N.J.; Newman, R.C. *Corros. Sci.* **1997**, *39*, 1771-1790

[6] Gollapudi, S. *Corros. Sci.* **2012**, *62*, 90-94.

[7] Strehblow, H-H.; Wenners, J. *Electrochim. Acta* **1977**, *22*, 421-427.

[8] Strehblow, H-H. Habilitationsschrift, Freie Universitat, Berlin, 1977.

[9] Schwenk, W. *Corrosion*, **1964**, *20*, 129-137.

[10] Sato, N. In *Corrosion and Corrosion Protection;* Frankenthal, R.P.; Mansfeld, F. Eds.; The Electrochemical Society: Pennington, 1981; pp 110-122.

[11] Sato, N. *Corrosion Science*, **1995**, *37*, 1947-1967.

[12] Frankel, G.S.; Stockert, F.; Hunkeler, F.; Boehni, H. *Corrosion*, **1987**, *43*, 429.

[13] Chao, C.Y.; Lin, L.F.; Macdonald, D.D. *J. Electrochem. Soc.* **1981**, *128*, 1187.

[14] Ahn, S.; Kwon, H.; Macdonald, D.D. *J. Electrochem. Soc*. **2005**, *152*, B482-B490.

[15] Lu, P.; Engelhardt, G.L.; Kursten, B.; Macdonald, D.D. *J. Electrochem. Soc*., **2016**, *165*, C156.

CHAPTER 5

Summary, Conclusions and Future Considerations

5.1 Summary

In situ optical microscopy is a useful tool for observing the electrode surface during electrodissolution. In potentiostatic experiments where $E > E_p$ pits were nucleated shortly after the application of potential and nucleation subsided at early times. Pits began to undercut the bulk metal at early times. For $E > 0.6$ V pits were electropolished and produced an electrode current density greater than 3 A dm^{-2}.

In galvanostatic experiments at 0.4 A dm^{-2}, a large number of pits were nucleated at short times, but in order to maintain a constant current the growth rate was slowed throughout their lifetime. This caused most pits to repassivate at early times but a small population of pits attained temporary stability and continued to propagate. Because they were initially hemispherical, the constant number of propagating pits must have decreasing pit stability products in order to give a constant current. Under these conditions, as time progresses they may eventually propagate as crystallographic etch pits which likely contribute to residue. In most experiments, the eventual repassivation of the crystallographic etch pits necessitated subsequent nucleation.

Analysis of the current transients for a potential pulse to $E > E_p$ showed two distinct regions of pit growth; an early time region where the current increased according to t^2 and a later time growth region where current increased according to $t^{1/2}$. Both growth regions correspond to hemispherical pit growth. The onset of the $t^{1/2}$ regime in the current transient does not necessarily signal the loss of a pit cover, but merely a point at which it *could* be lost without observing a change in the rate. Potential pulse sequences designed to stop pit growth prior to the onset of $t^{1/2}$ growth were executed for 10^4 cycles and led to electrode surfaces that were unique when compared to potentiostatic or galvanostatic dissolution. The surfaces were free of significant metal undercutting and contained a mix of grain boundary dissolution and hemispherical pitting that depended on the pulse time. For pulse times shorter than the onset of the t^2 growth regime, the surface showed superficial dissolution that was preferential at grain boundaries. For pulse times that extended into the t^2 growth regime, the electrode surfaces were covered by hemispherical pits.

A pulse time of 50 ms, which corresponded to the superficial growth region of the transient, was used to evaluate anode residue and compare with galvanostatic dissolution. By choosing the appropriate pulse sequence with a 60 ms, 0 V phase (45% duty cycle), the electrode current density for the 50 ms pulse time (0.33A dm^{-2}) closely matched that of a galvanostatic experiment (0.36 A dm^{-2}). Repeat trials that sampled 16 pellets for each method showed that the 50 ms potential pulse cycle produced on average, 6.5 fold less anode residue.

5.2 Conclusions

Anode residue from Ni electrodissolution in Watts' electrolyte has two likely sources; lacy-pit covers and crystallographic etch pit interiors. By controlling two important factors; the electrode potential and the pit growth time, both of these sources have been reduced or eliminated in laboratory scale experiments. Regardless of the pit lifetime, it is important to maintain a large electrode potential to avoid crystallographic etch pitting. The main danger associated with galvanostatic dissolution is the decaying potential that must counteract $t^{1/2}$ growth to maintain a constant current from a constant number of corrosion pits. In this case, the pit stability product slowly decreases which in turn means that the concentration of corrosion products at the pit surface also decreases. Pits can then propagate for prolonged times as crystallographic etch pits with surface concentrations of corrosion products that are between the saturation concentration and the critical concentration. In simple terms, a constant number of pits, growing at low pit current density and decaying potential ($E < 0.6$ V) should be avoided, especially over long times.

There are two reasons to control the pit lifetime; to control the average current density while maintaining a large electrode potential, and to stop the pit growth prior to significant metal undercutting. With a fixed pulse potential and time, a desired average current can be readily achieved by adjusting the duty cycle. Stopping a population of pits from undercutting the bulk metal is not so trivial because the status of metal undercutting cannot be inferred from the current transient. However, it was established empirically that for $E > 1.0$ V, a growth time of 2 s resulted in mostly open hemispheres, many with electropolished interiors. Since a 2 s pit lifetime corresponded to the early stages of the $t^{1/2}$ growth regime, metal undercutting of hemispherical pits should be avoided for $E > 1.0$ V if the pit lifetime is cut short of the $t^{1/2}$

region. In general, a dense population of pits nucleated by repeated steps to sufficiently large potential and allowed to grow for t < 2 s should mitigate residue.

5.3 Future Considerations

5.3.1 Limitations of Method Variables

The potential pulsed dissolution method described in this thesis has essentially three variables that may be controlled, the pulse potential, the pulse time and the duty cycle. However, the duty cycle should not be considered independent because to attain a desired current density, it will be nearly fixed for a given pulse potential and time. The lowest usable potential is probably considerably anodic of E_p, because E_p= 0.32 V and pit propagation at E < 0.45 V resulted in crystallographic etch pits. Potentials in the range of 0.6 - 0.8 V should be evaluated for residue, specifically with longer pulses due to the delayed onset of the t^2 to $t^{1/2}$ transition. The upper potential limit is dictated by the increasing rates of competing reactions. As the potential approached 2 V the shape of the transient changed considerably, which was attributed to significant contributions to the current from competing reactions. In practice, Ni dissolution should supply 100% of the current and the pulse potential should probably be limited to E < 1.5 V. Usable pulse times should be long enough to generate a significant amount of Ni dissolution current but shorter than the onset of metal undercutting for hemispherical pits. Neither limiting time was determined in this work, but for E = 1.2 V, the range of 50 ms to 2 s falls within these limits.

For a given potential and pulse time, the duty cycle is used to control the average current density. The maximum duty cycle for any potential and pulse time is limited by the diffusion of corrosion products away from the pit during the 0 V phase. It is important that all pits repassivate between pulses because their continued growth from pulse-to-pulse gives a situation similar to galvanostatic dissolution where pits grow continuously, but at a lower current density. It was established in Chapter 2 that the repassivation of pits in Ni could be satisfactorily addressed by considering the diffusion coefficient of the metal ion, D, and the pit radius, r, according to Equation 5.1.[1,2]

$$t_r = \frac{r^2}{2D} \qquad [5.1]$$

To approximate the minimum repassivation time for a specific pulse time, the largest pit radius measured by WLIM was used. For a pulse time of 700 ms, the largest hemispherical pit was measured to have a radius of about 1 μm. Using an approximated diffusion coefficient of 10^{-5} cm^2 s^{-1}, the calculated repassivation time is around 0.5 ms. Ideally, the off phase should be many times longer than the repassivation time because t_r indicates a concentration drop below the critical concentration. As the concentration of corrosion products within the pit becomes closer to that of the bulk, the probability of nucleation within or in the vicinity of a repassivated pit decreases.

5.3.2 Scalability

There are several factors to consider for the use of the potential pulse method described within this thesis in larger scale electroplating and two will be addressed briefly here; effect of increased electrode areas, and the introduction of a Ti basket. The effect of scale-up on the electrode charging time will be considered for a simple geometry, two disk electrodes of identical size.

The time dependence of the electrode potential, *E(t)* after a potential step varies with Equation 5.2 where R_sC_e is the product of the electrode capacitance and the resistance in close proximity to the anode.[3]

$$E(t) = E(1 - e^{-t/R_sC_e}) \qquad [5.2]$$

The quantity R_sC_e, having units of time, is called the time constant and $5*R_sC_e$ is used as a benchmark to determine the charging time for the electrical double-layer. The electrode/solution interface has a specific interfacial capacitance, C_i, which has units of capacitance per unit area. For a disk electrode the overall electrode capacitance, C_e is then dependent on the electrode radius, as shown in Equation 5.3.[3]

$$C_e = \pi r^2 C_i \qquad [5.3]$$

The resistance of the solution between two disk electrodes of the same size is given by Equation 5.4 where *l* is the distance between them, κ is the solution conductivity and πr^2 is the cross sectional area of the cylindrical uniform current path between the electrodes (ie the electrode surface area).[3]

$$R_s = \frac{l}{\kappa \pi r^2} \qquad [5.4]$$

By combining equations 5.3 and 5.4, the quantity R_sC_e should then only depend on the specific interfacial capacitance, solution conductivity and the current path length according to Equation 5.5. The charging time is then predicted to remain constant as the electrode sizes are increased, if the geometry of the system does not change.

$$R_sC_e = \frac{lC_i}{\kappa} \qquad [5.5]$$

If electrode geometries change, this definition of the time constant is not valid. However, large changes in the time constant are not expected for different geometries providing the ratio of the areas and the distance between the electrodes are not significantly altered by scale-up.

The effects of introducing a Ti basket to the plating circuit are complex and should be investigated. One would expect a change in the electrode charging time due to the introduction of additional Ti/electrolyte interface, which provides a higher surface area and different specific interfacial capacitance. In addition the Ti basket will introduce circuit resistances, both from contact resistance between the basket and Ni, and from the increased resistance of the Ti basket itself. As a result, a smaller portion of the total potential difference between the anode and cathode will be found across the Ni/NiO/electrolye interface. This would be expected to affect pit nucleation and ohmic growth. Transients should be collected with a Ti basket to determine if there are any major differences in the onset of pit growth regimes, transient shape or pit morphology.

5.3.3 Cathode Deposit

Electrodeposition using a pulsed current has been used in commercial electroplating since the 1970s and the effect of pulsed deposition on the cathode deposit has been discussed in the literature.[4,5,6] Virtually all instances of pulsed electrodeposition in the literature apply a current pulse, which differs from the potential pulse described in this thesis. However, this literature provides a basis for discussion of the effect of potential pulses at the cathode. The main reason to use a pulsed current is that short pulse times permit very high current densities that are well above the diffusion-limited current density. High current densities require that the polarization be correspondingly high, which drives the nucleation of crystals over the growth of existing crystals leading to nanocrystalline deposits.[5,6] Since the pulsed potential method utilizes highly

controlled potentials, the polarization is not expected to differ greatly from that of galvanostatic deposition at similar potentials.

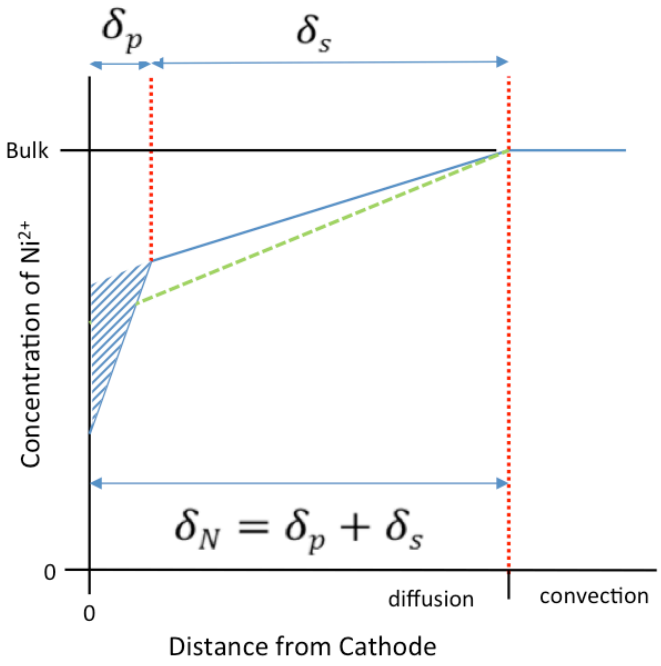

Figure 5-1: Diagram of the diffusion bilayer near the cathode formed by a pulsating current. The green line represents the diffusion layer during direct current depositon at the same current density. Pulsating and steady-state diffusion layer are indicated by δ_p and δ_s respectively. The triangular area close to the cathode represents the limits of the pulsating layer.

Ibl researched the effect of pulsed current deposition at the cathode and discussed in detail the diffusion layers.[5] The diffusion gradient was treated in two parts, both assumed to be linear, a quasi-steady state and a steady state region which are depicted in Figure 5-1. The separation of the diffusion zone into a bilayer can be rationalized by considering the two initial pulses. During the first pulse there is a drop in concentration at the cathode causing a diffusion gradient. The concentration of Ni^{2+} in this initial gradient is restored during the off phase but does not completely equilibrate with the bulk solution. In addition, the diffusion of species into the initial diffusion layer during the off time causes another gradient to develop outside of the initial gradient, generating a bilayer. The outer layer reaches a steady state in a few seconds and its

thickness is indicated in Figure 5-1 by δ_s. A steeper gradient is located nearer to the cathode that pulsates with the pulsating current, but always between the same values once the outer layer reaches a steady-state. The inner pulsating layer fluctuates in the area bound by the triangular space near the cathode surface in Figure 5-1 and its thickness is indicated by δ_p. The idea of two linear gradients implies that there exists a clear separation between them at a specific distance from the cathode. This is an over-simplification. There is actually a continuous dampening of the oscillations further from the cathode. For an approximation of the effect of potentiostatic pulses on the cathode, this simplified model should suffice.

Interestingly, the thickness of the inner diffusion layer, δ_p, given by Equation 5.6 depends only on the diffusion coefficient, D, the pulse time, T_p, and the total cycle, θ. The depletion at the cathode surface during a pulse Δc_c, given by Equation 5.7 is dependent on the pulse current density, j_p, pulse time and the diffusion coefficient. To find the maximum depletion at the cathode surface for a given pulse sequence, one must approximate the total thickness of the diffusion bilayer and calculate the concentration drop at the plane between the inner and outer diffusion layers, Δc_p according to Equation 5.8.

$$\delta_p = \left[2DT_p \left(1 - \frac{T_p}{\theta} \right) \right]^{\frac{1}{2}} \qquad [5.6]$$

$$\Delta c_c = \frac{2 j_p T_p}{\delta_p Z_m F} \qquad [5.7]$$

$$\Delta c_p = \frac{j_p}{Z_m F D} \frac{T_p}{\theta} (\delta_N - \delta_p) \qquad [5.8]$$

Using Equations 5.6 through 5.8, the diffusion bilayer near the cathode can be approximated for a 1.2 V, 50 ms, 45% duty cycle pulse sequence. For this sequence, the average anode current density was around 0.33 A dm^{-2}. Since the duty cycle was 45%, the average anode current density during the pulse should be around 0.7 A dm^{-2}. If the cathode is reasoned to be about one quarter of the anode surface area, then the average cathode current density during the pulse should be around 2.8 A dm^{-2}. Using Equation 5.6 with an approximate diffusion coefficient of 10^{-5} cm^2 s^{-1}, the thickness of the inner quasi-steady-state diffusion layer is calculated to be around 7 μm. Using this value and Equation 5.7, the drop in concentration of Ni^{2+} at the cathode

surface during each pulse is about 0.02 M. To find the minimum concentration at the cathode surface for this pulse sequence the total thickness of the diffusion bilayer was approximated to be 300 μm and the concentration drop at the plane that separates the two diffusion layers was calculated using Equation 5.8 to be around 0.2 M. In this case, the drop in Ni^{2+} concentration at the cathode surface is around 0.22 M compared to the bulk solution. The drop occurs over two diffusion gradients, an outer steady state layer which drops 0.2 M over approximately 293 μm and an inner fluctuating layer that drops about 0.02 M over approximately 7 μm. The total concentration drop at the cathode represents less than 20% of the total Ni^{2+} in the bulk plating solution. Since the pulsating layer is small and the total concentration drop over the diffusion bilayer is a property of the average current density, the cathode deposit is not expected to vary significantly from that attained during direct current deposition at a similar current density.

In conclusion, the research presented in this thesis has shown that on a small laboratory scale, the morphology of anode dissolution can be altered in a way that reduces residue. Any dissolution method that avoids extended periods of metal undercutting and crystallographic etch pitting should mitigate residue based on the conjectures made herein. The widespread adoption of potential pulse dissolution to mitigate residue in commercial plating requires subsequent research to determine if the pitting of Ni p-pellet in contact with a Ti basket can be similarly controlled. If this can be achieved, other factors such as electrode charging and properties of the cathode deposit, to a first approximation, should not be adversely affected by the pulsed method. The method is therefore promising to mitigate anode residue in Watts' electrolyte plating cells operated at low anode current densities.

5.4 References

[1] Strehblow, H-H.; Marcus, P. Mechanisms of Pitting Corrosion. In *Corrosion Mechanisms in Theory and Practice*; Marcus, P., Ed.; CRC Press, Boca Raton, USA, 2011; pp 349-393.

[2] Strehblow, H-H. *Werkst. Korros.* **1976**, *27*, 792.

[3] Bard A.J.; Faulkner, L.R. *Electrochemical Methods: Fundamentals and Applications*; Wiley, New York: 2001.

[4] Osero, N.M. *Plating and Surf. Finishing*, **1986**, *March*, 20-22.

[5] Ibl, N. *Surface Technology*, **1980**, *10*, 81-104.

[6] Popov, K.I.; Pavlovic, M.G.; Removic, G.Z. *J. Appl. Electrochem.,* **1991**, *21*, 743-745.